Editors' Suggestion

Regularized Stokeslet rings: An efficient method for axisymmetric Stokes flow with application to the growing pollen tube

J. Tyrrell, D. J. Smith, and R. J. Dyson*
School of Mathematics, University of Birmingham, Edgbaston, Birmingham B15 2TT, United Kingdom

(Received 28 February 2019; published 6 June 2019)

The method of regularized Stokeslets, based on the divergence-free exact solution to the equations of highly viscous flow due to a spatially smoothed concentrated force, is widely employed in biological fluid mechanics. Many problems of interest are axisymmetric, motivating the study of the azimuthally integrated form of the Stokeslet which physically corresponds to a ring of smoothed forces. The regularized fundamental solution for the velocity (single-layer potential) and stress (double-layer potential) due to an axisymmetric ring of smoothed point forces, the regularized ringlet, is derived in terms of complete elliptic integrals of the first and second kind. The relative errors in the total drag and surrounding fluid velocity for the resistance problem on the translating, rotating unit sphere, as well as the condition number of the underlying resistance matrix, are calculated; the regularized method is also compared to three-dimensional regularized Stokeslets and the singular method of fundamental solutions. The velocity of Purcell's toroidal swimmer is calculated; regularized ringlets enable accurate evaluation of surface forces and propulsion speeds for nonslender tori. The benefits of regularization are illustrated by a model of the internal cytosolic fluid velocity profile in the rapidly growing pollen tube. Actomyosin transport of vesicles in the tube is modeled using forces immersed in the fluid, from which it is found that transport along the central actin bundle is essential for experimentally observed flow speeds to be attained. The effect of tube growth speed on the internal cytosolic velocity is also considered. For axisymmetric problems, the regularized ringlet method exhibits a comparable accuracy to the method of fundamental solutions while also allowing for the placement of forces inside of the fluid domain and having more satisfactory convergence properties.

DOI: 10.1103/PhysRevFluids.4.063102

I. INTRODUCTION

The Stokes equations for incompressible flow at zero Reynolds number are used extensively to model the viscous-dominated regime of microscale flows, particularly biological flows associated with cilia-driven transport, and the motility and feeding of flagellated cells such as bacteria, spermatozoa, algae, and choanoflagellates. For an overview, see Ref. [1]. The fundamental solution of the Stokes flow equation, which corresponds to the flow driven by a single spatially concentrated force, is often referred to as the Oseen tensor or Stokeslet. The linearity of the Stokes flow equations enables the construction of solutions to problems involving moving boundaries with complex geometry through integral sums of Stokeslets, forming the basis for the method of fundamental solutions, slender body theory, and boundary integral methods. The latter numerical method has the principle major advantage of avoiding the need to mesh the fluid volume, which has enabled highly accurate and efficient simulation of biological flow systems for several decades [2–4]. Indeed, more

*Corresponding author: r.j.dyson@bham.ac.uk

approximate methods based on line distributions of Stokeslets and higher-order singularities also enabled major progress in this area before the present era of computationally intensive research. For a review see the earlier work of Chwang, Wu, and co-workers [5], who also explore a wide range of applications as part of a series of papers on low-Reynolds-number flow [6–10].

Nevertheless, two implementational issues arise with methods based on singular solutions. The first is that boundary integrals of solutions with a $1/r$-type singularity can be technically complex to evaluate on or near the boundary. Line integrals associated with models of slender bodies such as cilia and flagellar are "more singular" and can require careful distinction between the inside and outside of the body. Moreover, there are cases in which immersed forces due to, e.g., many suspended moving particles are desired to be modeled by an immersed volumetric force. Cortez *et al.* developed the method of regularized Stokeslets [11,12] based on the exact divergence-free solution to the Stokes flow equations due to a concentrated but spatially smoothed (regularized) force. This approach has enabled the use of Stokeslet methods in a wider range of applications, such as those in which an inducing force is present in the interior of the fluid domain (as either a point in $\mathbb{R}^2$ or a point or curve in $\mathbb{R}^3$).

While conceptually elegant, the standard implementation of the method of regularized Stokeslets is computationally expensive, motivating the development of boundary element discretization [13], line integration [14], and meshless interpolation [15] among other approaches. Many diverse biological flow problems of interest exhibit rotational symmetry, examples including spherical squirmer swimmers [16], the conceptual toroidal swimmer of Purcell [17], and cytosolic flow in elongating pollen tubes [18]. Thus motivated, in this paper we study axisymmetric Stokes flows in which the singular and regularized Stokeslets can be integrated azimuthally to yield an axisymmetric ring of point forces. The singular solution to this problem is already known [19]; the regularized solution, which we term the regularized ringlet, is newly derived. This solution forms the basis for an efficient axisymmetric method of regularized Stokeslets.

We begin in Sec. II by introducing the singular and regularized Stokeslets and review their application in solving the resistance problem for a rigid body translating in a viscous fluid. The derivation of the regularized ringlet is given in Sec. II A, with the analytical solution following in Sec. II B. The double-layer potential, relevant to bodies undergoing volume-changing deformation, is considered in Sec. II C, with analytical evaluation of the azimuthal integral in the double-layer potential given in Appendix D. A brief description of the computational efficiency of the method of regularized ringlets is given in Sec. II D, with a more thorough analysis in Appendix G. Possible modifications to the method using a different choice of cutoff function (for regularization) are considered in Sec. II E. In Sec. III, the method of regularized ringlets is applied to simple test cases such as the resistance problem for the translating (Sec. III A) and rotating (Sec. III B) sphere. The case of Purcell's toroidal swimmer [17,20] is also considered (Sec. III C), in which the method of regularized ringlets enables the calculation of propulsion speeds which are in excellent agreement with analytical results for both slender and nonslender tori. We then present a study of fluid flow in the angiosperm pollen tube in Sec. IV, an illustrative example highlighting the benefits of being able to apply smoothed forces inside the fluid (two prominent features of regularization). The velocity profiles we obtain for cytosolic flow in the tube are a close match to experimental results and provide fresh insight into the organization of the tube's internal transport systems. In Sec. V we conclude with a summary of results and a discussion of future work.

II. SINGULAR AND REGULARIZED STOKESLET SOLUTIONS

For the viscous-dominated very-low-Reynolds-number flow associated with microscopic length scales and slow velocities, incompressible Newtonian flow is well approximated by the steady Stokes flow equations

$$\mu\nabla^2\mathbf{u} = \nabla p - \mathbf{F}, \tag{1}$$

$$\nabla \cdot \mathbf{u} = 0, \tag{2}$$

where μ is dynamic viscosity, p the pressure, $\mathbf{u}$ the velocity, and $\mathbf{F}$ the applied force per unit volume. In the case of a singular force of the form $\mathbf{F}(\mathbf{x}_0) = \mathbf{g}^p \delta(\mathbf{x}_0 - \mathbf{x})$ for arbitrary point force $\mathbf{g}^p$, arbitrary point $\mathbf{x}$ at which the singularity is located, and where δ is the Dirac delta function, the fundamental solution [21,22] for $\mathbf{u}$ (using Einstein summation convention here and throughout this paper) is given by

$$u_i(\mathbf{x}_0) = \frac{1}{8\pi\mu} S_{ij}(\mathbf{x}_0, \mathbf{x}) g_j^p, \tag{3}$$

where

$$S_{ij}(\mathbf{x}_0, \mathbf{x}) = \frac{\delta_{ij}}{|\mathbf{x}_0 - \mathbf{x}|} + \frac{(x_{0,i} - x_i)(x_{0,j} - x_j)}{|\mathbf{x}_0 - \mathbf{x}|^3} \tag{4}$$

is known as the Stokeslet (with δ_{ij} the Kronecker delta).

The singularity in the Stokeslet solution can be eliminated without loss of incompressibility by regularization of the force $\mathbf{F}$, as described by Cortez *et al.* [11,12]. The Dirac δ function is replaced with $\mathbf{F}(\mathbf{x}_0) = \mathbf{g}^p \phi_\varepsilon(\mathbf{x}_0 - \mathbf{x})$, where ϕ_ε is a radially symmetric, smooth cutoff function with the property $\int_{\mathbb{R}^3} \phi_\varepsilon(\mathbf{x}) d\mathbf{x} = 1$. This is in essence applying the force over a small ball, varying smoothly from a maximum at its center to approximately zero sufficiently far away, instead of using an infinite point force as in the classical Stokeslet solution. The numerical parameter ε dictates the radius of support of the force, and as $\varepsilon \to 0$ the classical solution is recovered. Solutions for $\mathbf{u}$ using regularized Stokeslets differ from those found using the singular Stokeslet only near the point where the force is applied. Following Cortez *et al.* [12], we take

$$\phi_\varepsilon(\mathbf{x}_0 - \mathbf{x}) = \frac{15\varepsilon^4}{8\pi(|\mathbf{x}_0 - \mathbf{x}|^2 + \varepsilon^2)^{7/2}}, \tag{5}$$

which yields

$$S_{ij}^\varepsilon(\mathbf{x}_0, \mathbf{x}) = \delta_{ij} \frac{|\mathbf{x}_0 - \mathbf{x}|^2 + 2\varepsilon^2}{(|\mathbf{x}_0 - \mathbf{x}|^2 + \varepsilon^2)^{3/2}} + \frac{(x_{0,i} - x_i)(x_{0,j} - x_j)}{(|\mathbf{x}_0 - \mathbf{x}|^2 + \varepsilon^2)^{3/2}}. \tag{6}$$

By considering a solid body D moving through the fluid, it can be shown that

$$\int_{\mathbb{R}^3} u_i(\mathbf{x}) \phi_\varepsilon(\mathbf{x}_0 - \mathbf{x}) dV(\mathbf{x}) = \frac{1}{8\pi\mu} \int_{\partial D} S_{ij}^\varepsilon(\mathbf{x}_0, \mathbf{x}) g_j^a dS(\mathbf{x}), \tag{7}$$

where $\mathbf{g}^a$ is the force per unit area exerted by the body surface (denoted by ∂D) on the surrounding fluid [12]. Equation (7) is exact; replacing the left-hand side with the velocity $u_i(\mathbf{x}_0)$ such that

$$u_i(\mathbf{x}_0) = \frac{1}{8\pi\mu} \int_{\partial D} S_{ij}^\varepsilon(\mathbf{x}_0, \mathbf{x}) g_j^a dS(\mathbf{x}) \tag{8}$$

introduces an error $O(\varepsilon^p)$, where $p = 1$ on or near the body surface and $p = 2$ sufficiently far away.

Discretizing Eq. (8) using N Stokeslets on the surface of the solid body D enables the approximation of the fluid velocity at any point $\mathbf{x}_0$ via a numerical quadrature formula

$$u_i(\mathbf{x}_0) = \frac{1}{8\pi\mu} \sum_{n=1}^{N} S_{ij}^\varepsilon(\mathbf{x}_0, \mathbf{x}_n) g_{n,j}^a W_n, \tag{9}$$

where $g_{n,j}^a$ denotes the jth component of the force per unit area applied at the point $\mathbf{x}_n$ (a Stokeslet location) and W_n is the quadrature weight associated with the nth particle. The value of W_n is dependent on the geometry of the body surface ∂D and in the work of Cortez *et al.* has units of area.

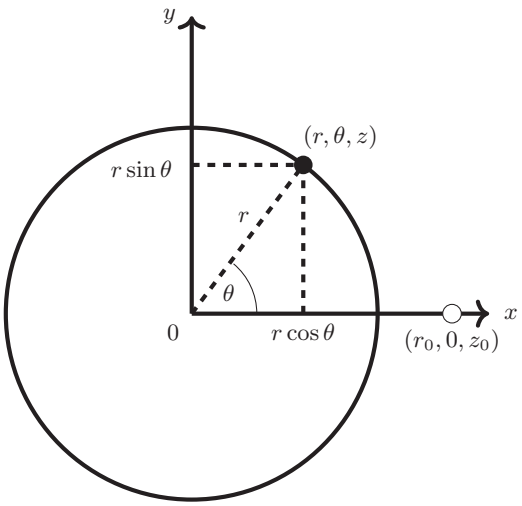

FIG. 1. Stokeslet ring in the (x, y) view. Note that the fluid point (open circle) and points on the ring (closed circle) do not necessarily both lie in the plane of the page (i.e., $z = z_0$ is not required).

A. Derivation of the regularized ringlet

Consider a specific case of Eq. (8) using a cylindrical (r, θ, z) coordinate system in which the body D exhibits rotational symmetry about the z axis. This symmetry enables analytical integration azimuthally, reducing the surface discretization to a line discretization and increasing accuracy. In doing so, we are effectively placing rings of regularized Stokeslets at positions $\mathbf{x}_n = (r_n, \theta, z_n)$ for $n = 1, \ldots, N$ and $\theta \in [0, 2\pi)$ (see Fig. 1 for a diagram of a single ring). This is analogous to covering the surface of the body in strips instead of the patches used in a standard three-dimensional (3D) Cartesian discretization. With a surface parametrization $\mathbf{x}(s, \theta)$, where $0 \leqslant s \leqslant \ell$ denotes arc length and $0 \leqslant \theta \leqslant 2\pi$, the boundary integral equation (8) reads

$$u_i(\mathbf{x}_0) = \frac{1}{8\pi\mu}\int_{\partial D} S_{ij}^{\varepsilon}(\mathbf{x}_0, \mathbf{x}) g_j^a(\mathbf{x}) dS(\mathbf{x}) = \frac{1}{8\pi\mu}\int_{s=0}^{\ell}\left(\int_{\theta=0}^{2\pi} S_{ij}^{\varepsilon}(\mathbf{x}_0, \mathbf{x}(s,\theta)) g_j^a(s,\theta) r(s) d\theta\right) ds. \tag{10}$$

Converting to cylindrical polar coordinates, we introduce the transformation matrix

$$\Theta(\theta) = \begin{pmatrix} \cos\theta & -\sin\theta & 0 \\ \sin\theta & \cos\theta & 0 \\ 0 & 0 & 1 \end{pmatrix}. \tag{11}$$

Letting indices i, j, k and α, β, γ correspond to Cartesian and cylindrical polar bases, respectively (such that $i = 1, 2, 3$ and $\alpha = 1, 2, 3$ correspond to x, y, z and r, θ, z, respectively, with Einstein summation convention employed for both sets), it follows that $g_j^a = \Theta_{j\alpha}(\theta) g_\alpha^a$. Assuming that velocity is evaluated at fluid point $\mathbf{x}_0 = (r_0, \theta_0, z_0)$ in cylindrical polar coordinates, it further follows that $u_i = \Theta_{i\alpha}(\theta_0) u_\alpha$. Recognizing that $\Theta^{-1} = \Theta^T$, substitution of the cylindrical forms of the velocity and force vectors into Eq. (10) thus yields

$$\begin{aligned} u_\alpha(r_0, \theta_0, z_0) &= \Theta_{\alpha i}(\theta_0) u_i(x_0, y_0, z_0) \\ &= \frac{1}{8\pi\mu}\Theta_{\alpha i}(\theta_0)\int_0^{\ell}\int_0^{2\pi} S_{ij}^{\varepsilon}(\mathbf{x}_0, \mathbf{x}(s,\theta))\Theta_{j\beta}(\theta) g_\beta^a(s) r(s) d\theta\, ds. \end{aligned} \tag{12}$$

Under the assumption of axisymmetry, it is sufficient to only consider cases $y_0 = \theta_0 = 0$. This results in the Cartesian x-z and the cylindrical polar r-z planes coinciding such that the transformation

matrix with $\theta_0 = 0$ simply yields the identity matrix (written as $\delta_{\alpha i} = 1$ when $\alpha = i$ and 0 otherwise in the summation) and Eq. (12) reduces to

$$u_\alpha(r_0, z_0) = \frac{1}{8\pi\mu}\int_0^\ell g_\beta^a(s)\left[\delta_{\alpha i} r(s)\int_0^{2\pi} S_{ij}^\varepsilon(\mathbf{x}_0, \mathbf{x}(s,\theta))\Theta_{j\beta}(\theta)d\theta\right]ds \tag{13}$$

$$= \frac{1}{8\pi\mu}\int_0^\ell g_\beta^a(s) R_{\alpha\beta}^\varepsilon(\mathbf{x}_0, \mathbf{x}(s))ds, \tag{14}$$

in which the ringlet kernel

$$R_{\alpha\beta}^\varepsilon(\mathbf{x}_0, \mathbf{x}(s)) := \delta_{\alpha i} r(s)\int_0^{2\pi} S_{ij}^\varepsilon(\mathbf{x}_0, \mathbf{x}(s,\theta))\Theta_{j\beta}(\theta)d\theta \tag{15}$$

is implicitly defined. Unlike the Stokeslet which has the symmetric property $S_{ij}^\varepsilon(\mathbf{x}_0, \mathbf{x}) \equiv S_{ij}^\varepsilon(\mathbf{x}, \mathbf{x}_0)$, ordering of arguments in the ringlet is important; the first and second arguments in $R_{\alpha\beta}^\varepsilon(\mathbf{x}_0, \mathbf{x})$ denote the fluid point and ring location, respectively, with the ring radius $r(s)$ being the crucial nonsymmetric term.

The various terms in the Stokeslet S_{ij}^ε can be evaluated in cylindrical polar coordinates via

$$x_{0,1} - x_1 = r_0 - r\cos\theta, \tag{16}$$

$$x_{0,2} - x_2 = -r\sin\theta, \tag{17}$$

$$x_{0,3} - x_3 = z_0 - z, \tag{18}$$

$$|\mathbf{x}_0 - \mathbf{x}|^2 = (r_0 - r\cos\theta)^2 + (r\sin\theta)^2 + (z_0 - z)^2. \tag{19}$$

The resulting form of each S_{ij}^ε is given in Appendix A and used in the evaluation of $R_{\alpha\beta}^\varepsilon$ in Eq. (15). These integrals $R_{\alpha\beta}^\varepsilon$ yield the regularized fundamental solution for an axisymmetric ring of concentrated force (the regularized ringlet). Analytical evaluation reveals that $R_{r\theta}^\varepsilon = R_{z\theta}^\varepsilon = R_{\theta r}^\varepsilon = R_{\theta z}^\varepsilon = 0$ such that the rotational problem for g_θ^a decouples from g_r^a and g_z^a. The remaining nonzero $R_{\alpha\beta}^\varepsilon$ yield the equations

$$\begin{pmatrix} u_r(\mathbf{x}_0) \\ u_z(\mathbf{x}_0)\end{pmatrix} = \frac{1}{8\pi\mu}\int_0^\ell \begin{bmatrix} R_{rr}^\varepsilon(\mathbf{x}_0, \mathbf{x}(s)) & R_{rz}^\varepsilon(\mathbf{x}_0, \mathbf{x}(s)) \\ R_{zr}^\varepsilon(\mathbf{x}_0, \mathbf{x}(s)) & R_{zz}^\varepsilon(\mathbf{x}_0, \mathbf{x}(s))\end{bmatrix}\begin{pmatrix} g_r^a(s) \\ g_z^a(s)\end{pmatrix}ds \tag{20}$$

and

$$u_\theta(\mathbf{x}_0) = \frac{1}{8\pi\mu}\int_0^\ell R_{\theta\theta}^\varepsilon(\mathbf{x}_0, \mathbf{x}(s)) g_\theta^a(s)ds. \tag{21}$$

Utilizing Eqs. (20) and (21) in tandem models axisymmetric problems with or without azimuthal rotation, in which the fluid experiences a constant force in each principal direction $(\hat{\mathbf{r}}, \hat{\boldsymbol{\theta}}, \hat{\mathbf{z}})$ at points along which the ringlet is located. This could be used, for example, to model the flow around a mobile axisymmetric body rotating about an axis defined by its direction of translation.

Approximating the integrals in Eqs. (20) and (21) numerically using a series of N rings yields a system of equations of the form

$$\begin{pmatrix} u_r(\mathbf{x}_0) \\ u_z(\mathbf{x}_0)\end{pmatrix} = \frac{1}{8\pi\mu}\sum_{n=1}^N \begin{bmatrix} R_{rr}^\varepsilon(\mathbf{x}_0, \mathbf{x}_n) & R_{rz}^\varepsilon(\mathbf{x}_0, \mathbf{x}_n) \\ R_{zr}^\varepsilon(\mathbf{x}_0, \mathbf{x}_n) & R_{zz}^\varepsilon(\mathbf{x}_0, \mathbf{x}_n)\end{bmatrix}\begin{pmatrix} g_r^a(\mathbf{x}_n) \\ g_z^a(\mathbf{x}_n)\end{pmatrix}w_n, \tag{22}$$

$$u_\theta(\mathbf{x}_0) = \frac{1}{8\pi\mu}\sum_{n=1}^N R_{\theta\theta}^\varepsilon(\mathbf{x}_0, \mathbf{x}_n) g_\theta^a(\mathbf{x}_n) w_n, \tag{23}$$

where $g_r^a(\mathbf{x}_n)$, $g_\theta^a(\mathbf{x}_n)$, and $g_z^a(\mathbf{x}_n)$ are the radial, azimuthal, and axial components of the forces per unit area applied at ringlet location $\mathbf{x}_n$, respectively, and w_n is the quadrature weight associated with $\mathbf{x}_n$ for numerical integration over s. The quantity w_n has units of length unlike its counterpart W_n in the work of Cortez *et al.* (units of length squared). It is also possible to combine the force per unit area $\mathbf{g}^a$ and quadrature weight w_n into a force per unit length $\mathbf{g}^l$ such that Eqs. (22) and (23) can alternatively represent the fluid velocity induced by a series of rings.

By considering the fluid velocity at each individual ringlet location, an invertible system can be produced. In the zero-azimuthal-velocity case ($u_\theta \equiv 0$), this takes the block matrix form

$$\mathsf{G}^l = 8\pi\mu \underbrace{\begin{bmatrix} \mathsf{R}^\varepsilon_{rr} & \mathsf{R}^\varepsilon_{rz} \\ \mathsf{R}^\varepsilon_{zr} & \mathsf{R}^\varepsilon_{zz} \end{bmatrix}^{-1}}_{\mathsf{R}^\varepsilon} \mathsf{U}, \tag{24}$$

where

$$\mathsf{G}^l = \begin{bmatrix} g_r^l(\mathbf{x}_1) \\ \vdots \\ g_r^l(\mathbf{x}_N) \\ g_z^l(\mathbf{x}_1) \\ \vdots \\ g_z^l(\mathbf{x}_N) \end{bmatrix}, \quad \mathsf{U} = \begin{bmatrix} u_r(\mathbf{x}_1) \\ \vdots \\ u_r(\mathbf{x}_N) \\ u_z(\mathbf{x}_1) \\ \vdots \\ u_z(\mathbf{x}_N) \end{bmatrix}, \tag{25}$$

and

$$\mathsf{R}^\varepsilon_{\alpha\beta} = \begin{bmatrix} R^\varepsilon_{\alpha\beta}(\mathbf{x}_1, \mathbf{x}_1) & R^\varepsilon_{\alpha\beta}(\mathbf{x}_1, \mathbf{x}_2) & \cdots & R^\varepsilon_{\alpha\beta}(\mathbf{x}_1, \mathbf{x}_N) \\ R^\varepsilon_{\alpha\beta}(\mathbf{x}_2, \mathbf{x}_1) & R^\varepsilon_{\alpha\beta}(\mathbf{x}_2, \mathbf{x}_2) & \cdots & R^\varepsilon_{\alpha\beta}(\mathbf{x}_2, \mathbf{x}_N) \\ \vdots & \vdots & \ddots & \vdots \\ R^\varepsilon_{\alpha\beta}(\mathbf{x}_N, \mathbf{x}_1) & R^\varepsilon_{\alpha\beta}(\mathbf{x}_N, \mathbf{x}_2) & \cdots & R^\varepsilon_{\alpha\beta}(\mathbf{x}_N, \mathbf{x}_N) \end{bmatrix}. \tag{26}$$

Hence the forces needed to induce a given prescribed velocity in the fluid may be found (the resistance problem). This works for both a series of translating rings and a translating axisymmetric body, with the force per unit length $\mathbf{g}^l$ essentially absorbing both the force per unit area $\mathbf{g}^a$ and the quadrature weight w_n in the latter case. Inclusion of azimuthal flow involves the formulation of a similar invertible system for Eq. (23) which can be solved separately.

B. Analytical evaluation of the regularized ringlet

The nonzero elements of the regularized ringlet can be expressed in the form

$$R^\varepsilon_{rr}(\mathbf{x}_0, \mathbf{x}_n) = r_n\{-r_0 r_n I_0 + [2\tau - (z_0 - z_n)^2]I_1 - 3r_0 r_n I_2\}, \tag{27}$$

$$R^\varepsilon_{rz}(\mathbf{x}_0, \mathbf{x}_n) = r_n(z_0 - z_n)(r_0 I_0 - r_n I_1), \tag{28}$$

$$R^\varepsilon_{zr}(\mathbf{x}_0, \mathbf{x}_n) = r_n(z_0 - z_n)(-r_n I_0 + r_0 I_1), \tag{29}$$

$$R^\varepsilon_{zz}(\mathbf{x}_0, \mathbf{x}_n) = r_n\{[\tau + (z_0 - z_n)^2 + \varepsilon^2]I_0 - 2r_0 r_n I_1\}, \tag{30}$$

$$R^\varepsilon_{\theta\theta}(\mathbf{x}_0, \mathbf{x}_n) = r_n[r_0 r_n I_0 + (\tau + \varepsilon^2)I_1 - 3r_0 r_n I_2], \tag{31}$$

in which $\tau := r_0^2 + r_n^2 + (z_0 - z_n)^2 + \varepsilon^2$ and

$$I_n := \int_0^{2\pi} \frac{\cos^n\theta}{(\tau - 2r_0 r_n \cos\theta)^{3/2}}\, d\theta \tag{32}$$

$$= \frac{4k^3}{(4r_0 r_n)^{3/2}} \int_0^{\pi/2} \frac{(2\cos^2\theta - 1)^n}{(1 - k^2\cos^2\theta)^{3/2}} d\theta, \tag{33}$$

with $k^2 := 4r_0 r_n/(\tau + 2r_0 r_n)$. Equation (33) is found by using the double-angle formula for $\cos\theta$ as well as symmetry arguments about $\pi/2$. Following the example of Pozrikidis [19], the integrals I_n can be computed by first expanding the numerator of the integrand in Eq. (33) to obtain a series of polynomial integrals with respect to $\cos\theta$. Letting

$$I_n' := 2^n \left(\frac{4k^3}{(4r_0 r_n)^{3/2}}\right) \int_0^{\pi/2} \frac{\cos^{2n}\theta}{(1 - k^2\cos^2\theta)^{3/2}} d\theta, \tag{34}$$

it follows that

$$I_0 = I_0', \quad I_1 = I_1' - I_0, \quad I_2 = I_2' - 2I_1' + I_0. \tag{35}$$

The individual integrals I_n' can be expressed in terms of complete elliptic integrals of the first and second kind, which are respectively defined

$$F = F(k) := \int_0^{\pi/2} \frac{d\theta}{(1 - k^2\sin^2\theta)^{1/2}}, \quad E = E(k) := \int_0^{\pi/2} (1 - k^2\sin^2\theta)^{1/2} d\theta. \tag{36}$$

The solutions for each I_n' (as can be found in Sec. 2.58 of Ref. [23]) are given by

$$I_0' = \frac{4k^3}{(4r_0 r_n)^{3/2}} \left(\frac{1}{1 - k^2} E\right), \tag{37}$$

$$I_1' = \frac{8k^3}{(4r_0 r_n)^{3/2}} \left(\frac{1}{k^2(1 - k^2)} E - \frac{1}{k^2} F\right), \tag{38}$$

$$I_2' = \frac{16k^3}{(4r_0 r_n)^{3/2}} \left(\frac{2 - k^2}{k^4(1 - k^2)} E - \frac{2}{k^4} F\right), \tag{39}$$

from which it follows that

$$I_0 = \frac{4k^3}{(4r_0 r_n)^{3/2}} \left(\frac{1}{1 - k^2} E\right), \tag{40}$$

$$I_1 = \frac{4k^3}{(4r_0 r_n)^{3/2}} \left(\frac{2 - k^2}{k^2(1 - k^2)} E - \frac{2}{k^2} F\right), \tag{41}$$

$$I_2 = \frac{4k^3}{(4r_0 r_n)^{3/2}} \left(\frac{k^4 - 8k^2 + 8}{k^4(1 - k^2)} E - \frac{4(2 - k^2)}{k^4} F\right). \tag{42}$$

Substitution of Eqs. (40)–(42) into Eqs. (27)–(31) yields the complete solution for the regularized ringlet

$$R_{rr}^{\varepsilon}(\mathbf{x}_0, \mathbf{x}_n) = \frac{k}{r_0 r_n} \left(\frac{r_n}{r_0}\right)^{1/2} \left[[\tau + (z_0 - z_n)^2] F + \frac{4r_0^2 r_n^2 - \tau[\tau + (z_0 - z_n)^2]}{\tau - 2r_0 r_n} E\right], \tag{43}$$

$$R_{rz}^{\varepsilon}(\mathbf{x}_0, \mathbf{x}_n) = k \frac{z_0 - z_n}{r_0} \left(\frac{r_n}{r_0}\right)^{1/2} \left[F + \frac{2r_0^2 - \tau}{\tau - 2r_0 r_n} E\right], \tag{44}$$

$$R_{zr}^{\varepsilon}(\mathbf{x}_0, \mathbf{x}_n) = -k \frac{z_0 - z_n}{(r_0 r_n)^{1/2}} \left[F + \frac{2r_n^2 - \tau}{\tau - 2r_0 r_n} E\right], \tag{45}$$

$$R^{\varepsilon}_{zz}(\mathbf{x}_0,\mathbf{x}_n) = 2k\left(\frac{r_n}{r_0}\right)^{1/2}\left[F + \frac{(z_0-z_n)^2+\varepsilon^2}{\tau - 2r_0r_n}E\right], \tag{46}$$

$$R^{\varepsilon}_{\theta\theta}(\mathbf{x}_0,\mathbf{x}_n) = \frac{k}{r_0r_n}\left(\frac{r_n}{r_0}\right)^{1/2}\left[(2\tau-\varepsilon^2)F + \frac{8r_0^2r_n^2+\tau(\varepsilon^2-2\tau)}{\tau-2r_0r_n}E\right]. \tag{47}$$

The solutions given by Eqs. (43)–(47) can be readily evaluated except when $r_0 = 0$ or $r_n = 0$. In the limit as $r_n \to 0$ (zero ring radius), all $R^{\varepsilon}_{\alpha\beta} \to 0$. In the limit as $r_0 \to 0$ (central fluid point), both R^{ε}_{zr} and R^{ε}_{zz} tend to finite values while $R^{\varepsilon}_{rr}, R^{\varepsilon}_{rz}, R^{\varepsilon}_{\theta\theta} \to 0$. This behavior is described in detail in Appendix B. Streamlines for the flow induced by the regularized ringlet with associated unit forces in both $\hat{\mathbf{r}}$ and $\hat{\mathbf{z}}$ directions are given in Appendix C.

The form of the ringlet solutions $R^{\varepsilon}_{\alpha\beta}$ is similar to those for the ring of singular Stokeslets (as detailed by Pozrikidis in [19] with the exception of the newly derived $R^{0}_{\theta\theta}$)

$$R^{0}_{rr}(\mathbf{x}_0,\mathbf{x}_n) = \frac{k}{r_0r_n}\left(\frac{r_n}{r_0}\right)^{1/2}\left[\left[r_0^2+r_n^2+2(z_0-z_n)^2\right]F - \frac{2(z_0-z_n)^4+3(z_0-z_n)^2\left(r_0^2+r_n^2\right)+\left(r_0^2-r_n^2\right)^2}{(z_0-z_n)^2+(r_0-r_n)^2}E\right], \tag{48}$$

$$R^{0}_{rz}(\mathbf{x}_0,\mathbf{x}_n) = k\frac{z_0-z_n}{r_0}\left(\frac{r_n}{r_0}\right)^{1/2}\left[F + \frac{r_0^2-r_n^2-(z_0-z_n)^2}{(z_0-z_n)^2+(r_0-r_n)^2}E\right], \tag{49}$$

$$R^{0}_{zr}(\mathbf{x}_0,\mathbf{x}_n) = -k\frac{z_0-z_n}{(r_0r_n)^{1/2}}\left[F - \frac{r_0^2-r_n^2+(z_0-z_n)^2}{(z_0-z_n)^2+(r_0-r_n)^2}E\right], \tag{50}$$

$$R^{0}_{zz}(\mathbf{x}_0,\mathbf{x}_n) = 2k\left(\frac{r_n}{r_0}\right)^{1/2}\left[F + \frac{(z_0-z_n)^2}{(z_0-z_n)^2+(r_0-r_n)^2}E\right], \tag{51}$$

$$R^{0}_{\theta\theta}(\mathbf{x}_0,\mathbf{x}_n) = \frac{k}{r_0r_n}\left(\frac{r_n}{r_0}\right)^{1/2}\left[2\left[r_0^2+r_n^2+(z_0-z_n)^2\right]F - \frac{4(z_0-z_n)^4+4(z_0-z_n)^2\left(r_0^2+r_n^2\right)+2\left(r_0^2-r_n^2\right)^2}{(z_0-z_n)^2+(r_0-r_n)^2}E\right], \tag{52}$$

and in the limit as $\varepsilon \to 0$ our solutions are equivalent to their singular counterparts. This can be verified by substitution of $\varepsilon = 0$ into $R^{\varepsilon}_{\alpha\beta}$ and is a result of the cutoff function ϕ_ε approaching a δ distribution as $\varepsilon \to 0$.

Equations (20), (21), and (43)–(47) provide the solution (to within regularization error) for the fluid velocity at any point due to the drag force per unit area on the surface of a generalized axisymmetric body. Using Eqs. (22) and (23) in place of (20) and (21) yields the numerical solution based on discretization over the arc length s. In the case of a single ring, removing the integral over s and replacing the force per unit area $\mathbf{g}^a$ with a force per unit length $\mathbf{g}^l$ yields the solution for the fluid velocity induced by the force acting along the ring in 3D space.

C. Double-layer potential

A more complete formulation of Eq. (7) for the fluid velocity induced by a translating body D is given by

$$\int_{\mathbb{R}^3} u_j(\mathbf{x})\phi_\varepsilon(\mathbf{x}_0-\mathbf{x})dV(\mathbf{x}) = \frac{1}{8\pi\mu}\int_{\partial D} S^{\varepsilon}_{ij}(\mathbf{x}_0,\mathbf{x})g^a_i(\mathbf{x})dS(\mathbf{x}) + \frac{1}{8\pi}\int_{\partial D} u_i(\mathbf{x})T^{\varepsilon}_{ijk}(\mathbf{x}_0,\mathbf{x})n_k(\mathbf{x})dS(\mathbf{x}), \tag{53}$$

where the first and second integrals on the right-hand side are known as the single-layer potential and the double-layer potential (DLP), respectively. The stress tensor T^{ε}_{ijk} present in the DLP is given

by

$$T^{\varepsilon}_{ijk}(\mathbf{x}_0,\mathbf{x}) = -6\frac{(x_{0,i}-x_i)(x_{0,j}-x_j)(x_{0,k}-x_k)}{(|\mathbf{x}_0-\mathbf{x}|^2+\varepsilon^2)^{5/2}} - 3\varepsilon^2\frac{(x_{0,i}-x_i)\delta_{jk}+(x_{0,j}-x_j)\delta_{ik}+(x_{0,k}-x_k)\delta_{ij}}{(|\mathbf{x}_0-\mathbf{x}|^2+\varepsilon^2)^{5/2}}. \tag{54}$$

The DLP can be neglected for problems in which the condition $\int_{\partial D}\mathbf{u}\cdot\hat{\mathbf{n}}\,dS=0$ is satisfied (see [19], Chap. 2.3), which is the case throughout this paper. However, we provide the expressions for the DLP in Appendix D, which may be of value for future studies of systems in which the condition $\int_{\partial D}\mathbf{u}\cdot\hat{\mathbf{n}}\,dS=0$ is violated (e.g., bubbles).

D. Efficiency and computational speed

A thorough comparison of the efficiency of the method of regularized ringlets with regularized Stokeslets for 3D problems with axisymmetry is given in Appendix G, with the results summarized here.

Two separate computational costs can be identified for solving resistance problems in Stokes flow: the cost associated with constructing the resistance matrix R^{ε} (or S^{ε}) and that associated with subsequent inversion of this matrix while finding a solution to the system of linear equations relating fluid velocity and force. For zero-azimuthal flow, R^{ε} is a matrix of size $2N\times 2N$ whereas S^{ε} is of size $3N\times 3N$. It might be expected that the cost of constructing R^{ε} is thus smaller than that of S^{ε} for a given number of nodes N, but in practice this is not the case; the additional cost of computing complete elliptic integrals $F(k)$ and $E(k)$ for all combinations of points $(\mathbf{x}_m,\mathbf{x}_n)\,\forall\, m,n\in 1,\ldots,N$, as well as $\mathsf{R}^{\varepsilon}_{\alpha\beta}$ not sharing an easy-to-encode common form for different combinations of $\alpha,\beta\in\{r,z\}$ in the same manner as $\mathsf{S}^{\varepsilon}_{i,j}$ for $i,j\in\{x,y,z\}$, means that it typically takes 10%–20% longer to construct R^{ε} than S^{ε}. However, the cost of constructing resistance matrices is generally insignificant compared to the cost of inversion for any number of nodes of practical use. In further testing, we found that solving a linear system $\mathbf{X}=\mathbf{A}\backslash\mathbf{b}$ (with $\mathbf{A}$ representing either R^{ε} or S^{ε}) was approximately three times faster using R^{ε} than S^{ε} for any given N (for all values of N tested). This performance advantage is further enhanced by the fact that (as shown in Appendix E) solutions for the resistance problem on the translating unit sphere using N nodes with regularized ringlets are consistently more accurate than solutions found using $3N^2/2$ nodes with regularized Stokeslets, suggesting that a drastic reduction in computational time can be achieved by using regularized ringlets for axisymmetric Stokes flow problems.

E. Other choices of cutoff function

The cutoff function used as part of the regularized Stokeslet (and thus the regularized ringlet) in this paper is not a unique choice; others can be used, as detailed by Cortez *et al.* [11,12]. In particular, for certain applications it may be preferable to use a cutoff function with compact support (as opposed to the infinitely supported function used here). Examples of compactly supported cutoff functions $\phi_\varepsilon(r)$ in the literature [24,25] are typically polynomial functions of the parameter $r^*=r/\varepsilon$ for $0\leqslant r^*\leqslant 1$ and 0 otherwise, yielding regularized Stokeslet solutions which are similarly polynomial for $0\leqslant r^*\leqslant 1$ and revert to the classical Stokeslet outside of this range. Analytical azimuthal integration of a regularized Stokeslet deriving from such a compactly supported cutoff function is thus straightforward, consisting solely of integration of powers of trigonometric functions for $0\leqslant r^*\leqslant 1$ and yielding the classical solution of Pozrikidis [19] for a ring of Stokeslets otherwise. With minor modifications, the method presented in this paper can thus be easily adapted to derive and utilize a regularized ringlet using a cutoff function with compact support.

TABLE I. Relative errors in the drag calculation for the resistance problem on the translating unit sphere.

ε	$N = 25$	$N = 51$	$N = 101$	$N = 201$	$N = 401$
0.01	-1.4689×10^{-2}	-2.0609×10^{-3}	1.6439×10^{-3}	2.4053×10^{-3}	2.5104×10^{-3}
0.005	-2.4754×10^{-2}	-7.2086×10^{-3}	-1.1116×10^{-3}	7.6816×10^{-4}	1.2056×10^{-3}
0.001	-4.7242×10^{-2}	-1.8774×10^{-2}	-7.0948×10^{-3}	-2.3160×10^{-3}	-5.1183×10^{-4}

III. SIMPLE EXAMPLES AND TEST CASES

In Sec. II the expression for the regularized fundamental solution for an axisymmetric ring of concentrated forces, the regularized ringlet, was derived. In the following, we demonstrate the validity of the method through application to simple cases of motion.

The first two cases concern the translation and rotation of the unit sphere in a Stokesian fluid, treated independently in Secs. III A and III B, respectively. In Sec. III C a more complicated example is considered: the propulsion of Purcell's toroidal swimmer [17,20], powered by tank treading of the torus surface. In considering these different cases, it is shown that the method of regularized ringlets can be used to model the surface motion of axisymmetric bodies in each principal direction $\hat{\mathbf{r}}$, $\hat{\boldsymbol{\theta}}$, and $\hat{\mathbf{z}}$ in a cylindrical coordinate system.

A. Translating unit sphere

The validity of the regularized ringlet method is illustrated by solving the resistance problem for the translating unit sphere. Given a prescribed surface velocity $(-\hat{\mathbf{z}})$, Eq. (14) yields a Fredholm first kind integral equation for the unknown force distribution [15]. The method of regularized ringlets (implemented here via MATLAB) can be used to solve this problem.

The sphere is parametrized in the r-z plane by $\mathbf{p} = \cos\varphi\,\hat{\mathbf{r}} + \sin\varphi\,\hat{\mathbf{z}}$ for $\varphi \in [-\pi/2, \pi/2]$ and then discretized as

$$\varphi_n = \pi\frac{n - 1/2}{N} - \frac{\pi}{2} \quad \text{for } n = 1, \ldots, N. \tag{55}$$

The velocity boundary condition $\mathbf{u} = -\hat{\mathbf{z}}$ is prescribed at each $\mathbf{x}_n := \mathbf{p}(\varphi_n)$, and the resulting linear system is solved to yield the required force densities $\mathbf{g}^l$ at each of these locations. The total drag exerted by the fluid on the sphere is then calculated as

$$-\sum_{n=1}^{N}\int_{\theta=0}^{2\pi} g_z^l(\mathbf{x}_n) r(\mathbf{x}_n) d\theta = -2\pi\sum_{n=1}^{N} r(\mathbf{x}_n) g_z^l(\mathbf{x}_n), \tag{56}$$

which is compared with the Stokes law value of 6π. The relative errors are given for various values of N and regularization parameter ε in Table I alongside the condition number of the resistance matrix R^ε in Table II.

TABLE II. Condition numbers of the resistance matrix R^ε for the resistance problem on the translating unit sphere.

ε	$N = 25$	$N = 51$	$N = 101$	$N = 201$	$N = 401$
0.01	4.6282×10^1	1.5857×10^2	7.1602×10^2	7.0167×10^3	4.0767×10^5
0.005	3.3089×10^1	9.6186×10^1	3.1303×10^2	1.4181×10^3	1.3947×10^4
0.001	1.9973×10^1	4.9332×10^1	1.2386×10^2	5.7653×10^2	1.0449×10^3

For given N, excessively small ε results in the drag error becoming nonmonotonic. For given ε, increasing N eventually ceases to result in a further reduction in the relative error. This is often the case with regularized Stokeslet methods (see, e.g., Figs. 15 and 16 and Refs. [12,26]).

A thorough comparison of our results for the translating unit sphere with those of Cortez *et al.* [12] can be found in Appendix E, in which it is found that using just N ringlets yields consistently more accurate solutions than using $3N^2/2$ regularized Stokeslets in a standard 3D discretization of the sphere surface. A comparison to results obtainable using the axisymmetric method of fundamental solutions (a singular Stokeslet method) is given in Appendix F, in which the relative error in the fluid velocity is also discussed. In general, although the singular method can be tuned to give smaller relative errors in either the fluid velocity or total drag separately, it cannot do so simultaneously; regularized ringlets display more satisfactory convergence properties and are the more effective method to minimize errors in both fluid velocity and total drag.

B. Rotating unit sphere

The solution for the steady motion of a Stokesian fluid surrounding a solid sphere rotating uniformly about a central axis is well known and can be found in, e.g., [27]. If the sphere rotates around its z axis in an (r, θ, z) cylindrical coordinate system with an angular velocity $\boldsymbol{\Omega} = \omega_0 \hat{\mathbf{z}}$, the resulting angular velocity of the fluid is given by $\boldsymbol{\omega} = (a/\gamma)^3 \omega_0 \hat{\boldsymbol{\theta}}$, where $\gamma = \sqrt{r^2 + z^2}$. This can be written in terms of the linear velocity (more readily usable in the Stokeslet formulas) over the entire domain as

$$\mathbf{u} = \begin{cases} r\left(\frac{a}{\gamma}\right)^3 \omega_0 \hat{\boldsymbol{\theta}} & \forall\, \gamma \geqslant a \\ r\omega_0 \hat{\boldsymbol{\theta}} & \forall\, \gamma < a, \end{cases} \tag{57}$$

where $\gamma \geqslant a$ corresponds to the surrounding fluid velocity and $\gamma < a$ to the solid body rotation of the sphere, respectively. The zero-Reynolds-number torque on this sphere is given by

$$\mathbf{T} = -8\pi\mu a^3 \boldsymbol{\Omega}, \tag{58}$$

the derivation of which can be found in [28]. This torque is associated with a drag force per unit area on the surface of the sphere given by $\mathbf{f} = -3\mu\omega_0(r/a)\hat{\boldsymbol{\theta}} = -\mathbf{g}^a$, as detailed in Appendix H. The force per unit length used in the method of regularized ringlets thus takes the form

$$g^l_\theta = \left(\frac{3\pi\mu}{N}\right)\left(\frac{r}{a}\right)\omega_0, \tag{59}$$

although for the resistance problem this is not prescribed.

The sphere surface is again parametrized in the r-z plane by $\mathbf{p} = \cos\varphi\, \hat{\mathbf{r}} + \sin\varphi\, \hat{\mathbf{z}}$ for $\varphi \in [-\pi/2, \pi/2]$, discretized using N ringlets at locations $\mathbf{x}_n$. Letting $\omega_0 = -1$, the velocity $\mathbf{u}(\mathbf{x}_n) = -r(\mathbf{x}_n)\hat{\boldsymbol{\theta}}$ is prescribed at each $\mathbf{x}_n$ and the resistance matrix is constructed to yield the required force densities $\mathbf{g}^l$ at each of these locations. The torque is then calculated as

$$-\sum_{n=1}^{N} \int_{\theta=0}^{2\pi} g^l_\theta(\mathbf{x}_n) r^2(\mathbf{x}_n) d\theta = -2\pi \sum_{n=1}^{N} r^2(\mathbf{x}_n) g^l_\theta(\mathbf{x}_n), \tag{60}$$

in which $r(\mathbf{x}_n)$ is squared since the torque is a moment, the product of distance and force. Comparing to the value 8π, relative errors are given for various values of N and regularization parameter ε in Table III alongside the condition number of the resistance matrix $\mathsf{R}^\varepsilon_\theta$ in Table IV. These results are similar to those of the translating unit sphere, although for given ε and N the relative error in the drag is generally slightly larger and the condition number of the resistance matrix slightly smaller than for the results using the same ε and N on the translating unit sphere.

TABLE III. Relative errors in the drag calculation for the resistance problem on the rotating unit sphere.

ε	$N = 25$	$N = 51$	$N = 101$	$N = 201$	$N = 401$
0.01	-6.6820×10^{-2}	-1.3919×10^{-2}	3.1012×10^{-3}	7.1409×10^{-3}	7.5502×10^{-3}
0.005	-1.0168×10^{-1}	-3.3360×10^{-2}	-7.2206×10^{-3}	1.5183×10^{-3}	3.5556×10^{-3}
0.001	-1.7339×10^{-1}	-7.5656×10^{-2}	-3.0238×10^{-2}	-1.0422×10^{-2}	-2.6879×10^{-3}

C. Purcell's toroidal swimmer

The torus is the simplest geometry capable of describing self-propelled organisms [29]. Purcell's toroidal swimmer [17,30] describes one such organism, the geometry of which can be seen in Fig. 2. Inward rotation of the torus surface produces a net force in the direction of motion of the outermost surface (against which the torus is propelled). The magnitude of this net force (and resultant propulsion speed of the torus) is dependent on the speed with which the surface of the torus rotates as well as the slenderness of the torus. It has been suggested that this mechanism could describe how a DNA miniplasmid could be turned into a self-propelled nanomachine [31]. Three modes of locomotion were considered by Leshansky and Kenneth [20], corresponding to tank treading of (a) an incompressible surface, in which the tangential surface velocity is largest on the inner surface, (b) a weakly compressible surface, in which the tangential surface velocity is constant, and (c) a highly compressible surface, in which the tangential surface velocity is largest on the outer surface. In the following, we restrict ourselves to looking at the case of constant tangential surface velocity.

The torus geometry is reduced to a single slenderness parameter $s_0 = b/a$, where b and a refer to the major and minor radii of the torus, respectively. The torus surface is parametrized in terms of angle $\eta \in [0, 2\pi)$ in the r-z plane such that $ds = ad\eta$ and $\eta = 0$ corresponds to the outermost radial point on the surface of the torus, traversed in the counterclockwise direction. For the free swimming torus, the rigid body translation $\mathbf{U}$ and rotation $\mathbf{u}^{(s)}$ of the torus surface ∂D are related to the force per unit area $\mathbf{g}^a$ exerted by the torus on the surrounding fluid by

$$U_\alpha(\mathbf{x}_0) + u_\alpha^{(s)}(\mathbf{x}_0) = \frac{1}{8\pi\mu} \int_{s=0}^{\ell} R^\varepsilon_{\alpha\beta}(\mathbf{x}_0, \mathbf{x}) g^a_\beta(\mathbf{s}) ds \, \forall \, \mathbf{x}_0 \in \partial D \tag{61}$$

subject to the condition of zero net force in the $\hat{\mathbf{z}}$ direction,

$$\int_{\partial D} \mathbf{g}^a_z(\mathbf{x}) dS(\mathbf{x}) = 0, \tag{62}$$

where s is the arc length parametrization of the cross section of the torus surface ∂D in the r-z plane. We note that the additional free swimming conditions of zero net force in $\hat{\mathbf{r}}$ and zero total moment (as outlined by Phan-Thien *et al.* [2]) are automatically satisfied by axisymmetry and $g^a_\theta \equiv 0$, respectively.

The propulsion speed $U := |\mathbf{U}|$ of the rotating torus for any given value of s_0 and rotation speed $u^{(s)} := |\mathbf{u}^{(s)}|$ can be determined by considering two separate situations: one in which motion is

TABLE IV. Condition numbers of the resistance matrix $\mathsf{R}^\varepsilon_\theta$ for the resistance problem on the rotating unit sphere.

ε	$N = 25$	$N = 51$	$N = 101$	$N = 201$	$N = 401$
0.01	7.7965	2.1678×10^1	7.1174×10^1	3.4925×10^2	4.2212×10^3
0.005	6.2313	1.5492×10^1	4.2389×10^1	1.4119×10^2	6.9613×10^2
0.001	4.4051	9.5164	2.1792×10^1	5.4064×10^1	1.4690×10^2

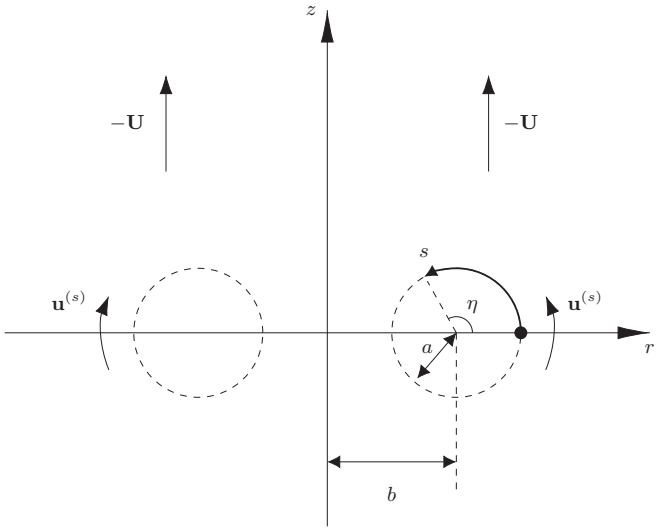

FIG. 2. Geometry of the toroidal swimmer, whose cross section in the r-z plane is given by the dashed lines. Rotation around the z axis produces the complete torus. The torus moves with velocity $\mathbf{U}$ in the direction opposing outer surface motion (such that, in the given frame of reference in which the torus remains stationary, the surrounding fluid appears to move with velocity $-\mathbf{U}$). Redrawn from Ref. [20].

purely translational in the $\hat{\mathbf{z}}$ direction (the toroidal glider with $\mathbf{U} = \hat{\mathbf{z}}$ and $\mathbf{u}^{(s)} \equiv \mathbf{0}$) and one in which motion is purely rotational (the anchored toroidal pump with $\mathbf{U} \equiv \mathbf{0}$ and $\mathbf{u}^{(s)} = \hat{\boldsymbol{\eta}}$, where $\hat{\boldsymbol{\eta}}$ is the unit vector whose direction varies over s, pointing tangential to the surface in the counterclockwise direction at all points). The glider and pump have associated force distributions $\mathbf{g}^{\mathrm{gld}}$ and $\mathbf{g}^{\mathrm{pmp}}$, respectively. Using the regularized ringlet, surface motions can be prescribed [Figs. 3(a) and 4(a)] in

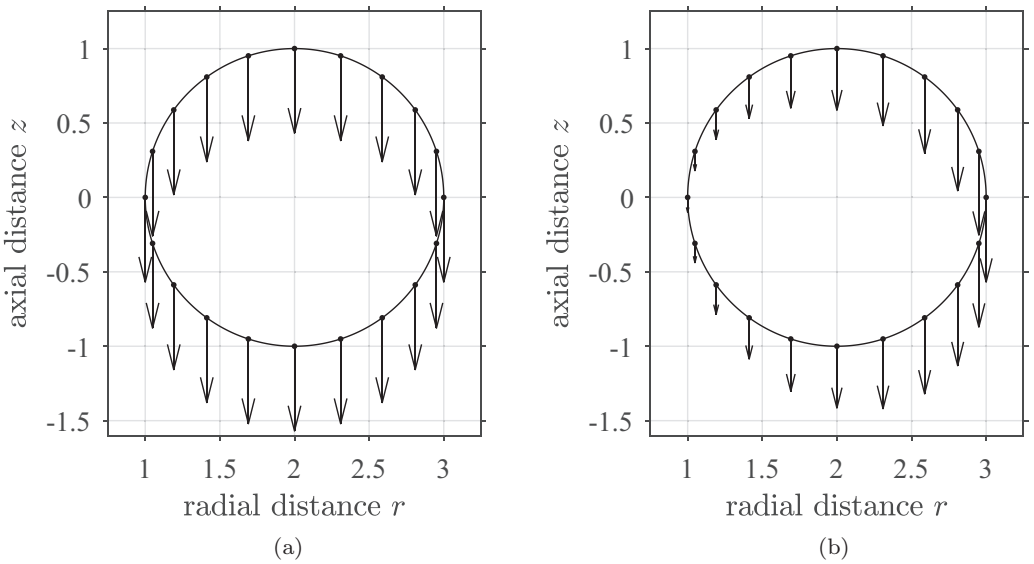

FIG. 3. (a) Surface velocity (broadwise translation of the torus) and (b) associated force distribution of a toroidal glider with slenderness parameter $s_0 = 2$.

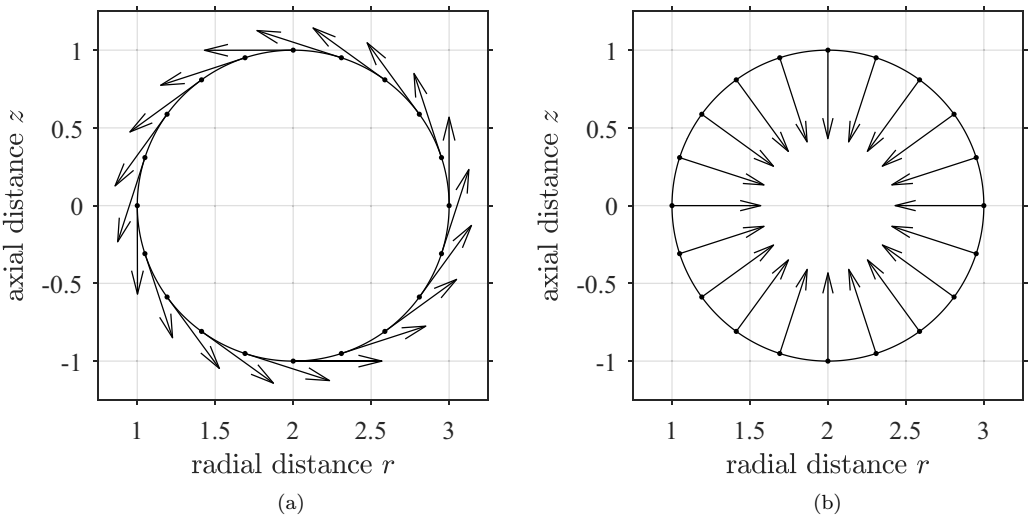

FIG. 4. (a) Surface velocity (counterclockwise surface rotation of the torus) and (b) associated force distribution of an anchored toroidal pump with slenderness parameter $s_0 = 2$.

order to compute the associated force distributions [Figs. 3(b) and 4(b)] responsible for producing each motion. For the toroidal glider the radial force is assumed to be zero ($g_r^{\mathrm{gld}} \equiv 0$); hence

$$U_r(\mathbf{x}_0) = \frac{1}{8\pi\mu}\int_{\eta=0}^{2\pi} R^{\varepsilon}_{rz}(\mathbf{x}_0,\mathbf{x}) g_z^{\mathrm{gld}}(\mathbf{x}) a\, d\eta = 0 \,\forall\, \mathbf{x}_0 \in \partial D, \tag{63}$$

$$U_z(\mathbf{x}_0) = \frac{1}{8\pi\mu}\int_{\eta=0}^{2\pi} R^{\varepsilon}_{zz}(\mathbf{x}_0,\mathbf{x}) g_z^{\mathrm{gld}}(\mathbf{x}) a\, d\eta = 1 \,\forall\, \mathbf{x}_0 \in \partial D, \tag{64}$$

which, after solving for the unknown force distribution $\mathbf{g}_z^{\mathrm{gld}}$, yields the net axial force in the $\hat{\mathbf{z}}$ direction

$$G^{\mathrm{gld}} = \int_{\partial D} g_z^{\mathrm{gld}}(\mathbf{x}) dS(\mathbf{x}), \tag{65}$$

which is nonzero. For the anchored toroidal pump the surface velocity is given by $\mathbf{u}^{(s)} = \hat{\boldsymbol{\eta}} = (-\sin\eta, \cos\eta)$ in (r, z) coordinates. It follows that

$$u_r^{(s)}(\mathbf{x}_0) = \frac{1}{8\pi\mu}\int_{\eta=0}^{2\pi} R^{\varepsilon}_{r\beta}(\mathbf{x}_0,\mathbf{x}) g_\beta^{\mathrm{pmp}}(\eta) a\, d\eta = -\sin\eta \,\forall\, \mathbf{x}_0 \in \partial D, \tag{66}$$

$$u_z^{(s)}(\mathbf{x}_0) = \frac{1}{8\pi\mu}\int_{\eta=0}^{2\pi} R^{\varepsilon}_{z\beta}(\mathbf{x}_0,\mathbf{x}) g_\beta^{\mathrm{pmp}}(\eta) a\, d\eta = \cos\eta \,\forall\, \mathbf{x}_0 \in \partial D, \tag{67}$$

from which it can be determined that the net axial $\hat{\mathbf{z}}$ force is given by

$$G^{\mathrm{pmp}} = \int_{\partial D} g_z^{\mathrm{pmp}}(\eta) dS(\mathbf{x}). \tag{68}$$

By linearity of the Stokes flow equations we may subtract the gliding solution from the pump solution to rewrite the system in the form

$$u_r^{(s)}(\mathbf{x}_0) = \frac{1}{8\pi\mu}\int_{\eta=0}^{2\pi} R^{\varepsilon}_{r\beta}(\mathbf{x}_0,\mathbf{x}) g_\beta^{a}(\eta) a\, d\eta \,\forall\, \mathbf{x}_0 \in \partial D, \tag{69}$$

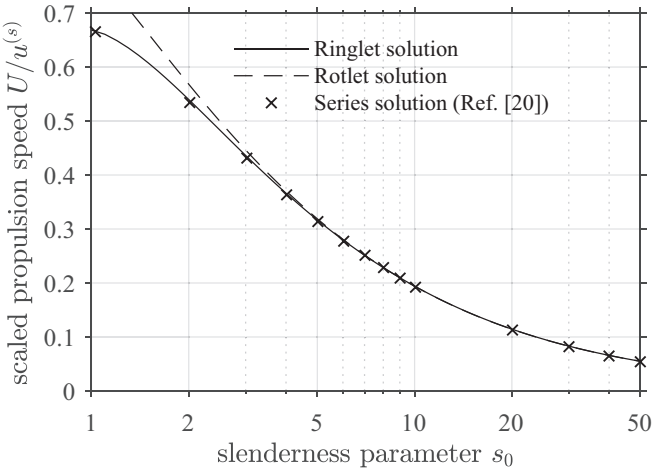

FIG. 5. Scaled propulsion speed $U/u^{(s)}$ versus slenderness parameter s_0 using different numerical schemes. The solid line shows the regularized ringlet solution using $N = 100$ rings (method derived in this paper). The dashed line shows the rotlet solution as detailed in [20]. The crosses denote values of the exact series solution, obtained from Fig. 7 of Ref. [20] using MATHWORKS' grabit function [32] in MATLAB.

$$-\frac{G^{\mathrm{pmp}}}{G^{\mathrm{gld}}} + u_z^{(s)}(\mathbf{x}_0) = \frac{1}{8\pi\mu}\int_{\eta=0}^{2\pi} R^{\varepsilon}_{z\beta}(\mathbf{x}_0, \mathbf{x}) g^a_\beta(\eta) a\, d\eta \;\forall\, \mathbf{x}_0 \in \partial D, \tag{70}$$

where $\mathbf{g}^a = \mathbf{g}^{\mathrm{pmp}} - (G^{\mathrm{pmp}}/G^{\mathrm{gld}}) g_z^{\mathrm{gld}} \hat{\mathbf{z}}$ and the net force is equal to

$$\int_{\partial D} g_z^a(\eta) dS(\mathbf{x}) = 0, \tag{71}$$

as required for the free swimmer. The propulsion velocity of the swimming torus is thus given by $\mathbf{U} = -(G^{\mathrm{pmp}}/G^{\mathrm{gld}})\hat{\mathbf{z}}$, opposing the direction of outer surface motion. The propulsion speed U is dependent on both the rotation speed $u^{(s)}$ and the slenderness ratio s_0, so both G^{gld} and G^{pmp} must be recomputed whenever one of these parameters is changed. However, Leshansky and Kenneth [20] were able to show that the propulsion speed depends linearly on the rotation speed such that by considering the scaled propulsion speed $U/u^{(s)}$ it is only necessary to vary s_0 to be able to consider all possible propulsion speeds resulting from a given constant rotational surface velocity.

Our results for the scaled propulsion velocity found using a discretization of the torus surface using $N = 100$ regularized ringlets are compared with those obtained by Leshansky and Kenneth [20], who tackled the same problem using a line distribution of rotlets at the torus centerline (inaccurate as $s_0 \to 1$) and an exact series solution via expansion in toroidal harmonics (Fig. 5). Of particular note, in the limit as $s_0 \to 1$, it is found that using $N = 100$ rings with $\varepsilon = 0.01$ in the regularized ringlet method yields a scaled propulsion velocity of 0.6684, representing just a 0.513% error when compared to the series solution value of 0.665. This error can be reduced to less than 0.1% by using $N = 1000$ rings, at which point the value of the scaled propulsion velocity as calculated by the method of regularized ringlets is 0.6656. This is a significant improvement over the solution found using a line distribution of rotlets, in which the error is greater than 1% for all $s_0 \leqslant 6$.

In addition to giving values for the scaled propulsion speed that are in excellent agreement with the series solution of Leshansky and Kenneth [20], the regularized ringlet solution also provides the force required at each point on the torus surface to produce the swimming motion. The series and rotlet solutions do not yield this information, with the propulsion speed instead being calculated

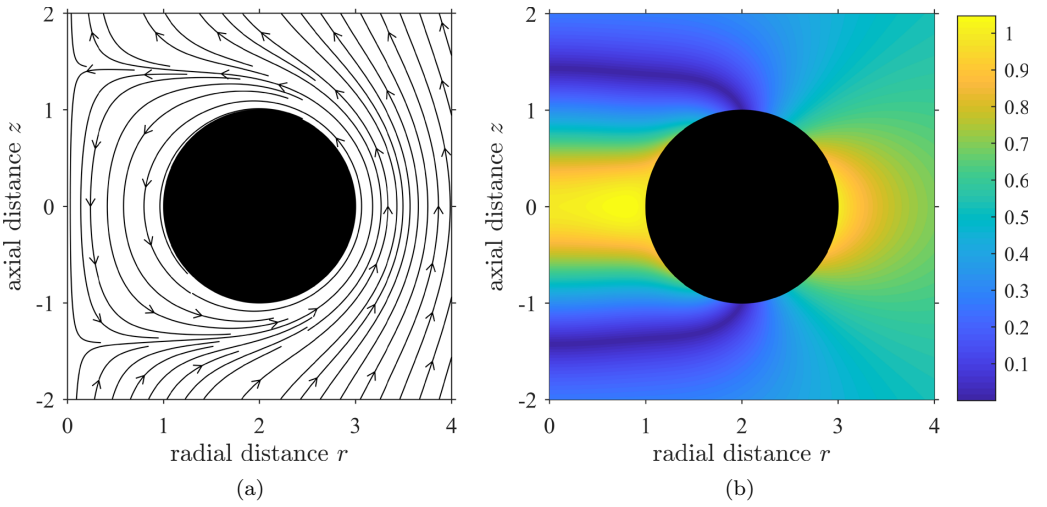

FIG. 6. (a) Streamlines and (b) magnitude of fluid velocity in the region surrounding the force-free toroidal swimmer with slenderness parameter $s_0 = 2$, undergoing uniform counterclockwise surface rotation with unit angular velocity. The torus propagates in the direction $-\hat{\mathbf{z}}$ and the frame of reference moves with the swimmer.

according to the net drag force on the toroidal glider in these methods. This, in combination with Figs. 3(a) and 3(b), highlights why the centerline rotlet solution is inaccurate for small values of s_0; as slenderness decreases, the difference between the magnitude of the force required at the innermost and outermost surfaces to produce rigid body translation of the torus grows large. In Fig. 3(b) (in which $s_0 = 2$), the drag force on the outer surface is approximately 5.7 times larger than that on the inner surface. The constant centerline force associated with the rotlet cannot account for this discrepancy, whereas the full discretization of the torus surface using regularized ringlets can.

Figures 6(a) and 6(b) show the streamlines and magnitude of the fluid velocity in a region near the force-free toroidal swimmer with slenderness parameter $s_0 = 2$, undergoing uniform counterclockwise surface rotation with unit angular velocity. This results in propagation of the torus in the direction $-\hat{\mathbf{z}}$. Fluid passing through the central hole of the torus is caught in closed streamlines, in agreement with the results of Leshansky and Kenneth [20].

IV. CYTOSOLIC FLOW IN THE POLLEN TUBE: AN ILLUSTRATIVE EXAMPLE OF THE BENEFITS OF REGULARIZATION

In Sec. III, the method of regularized ringlets was applied to simple cases of motion to illustrate validity and applicability. These canonical examples demonstrate the use of ringlets in situations with moving boundaries. However, perhaps the most important feature of the regularized method is the ability to place source points directly in the fluid, in which case the regularized ring represents a curve in 3D space. The regularization parameter ε can then be used to control the spreading of the force (the size of the region over which it is applied). This is useful in situations in which the exact location at which a force is applied in a fluid is unknown or when a force is applied over a large area. In the following, these features of regularization are explored in more detail by considering the example of fluid flow in the angiosperm pollen tube. A more extensive study of the biomechanics of pollen tube growth (with a particular focus on the transport and distribution of elements of the cytoplasm) is beyond the scope of the present paper.

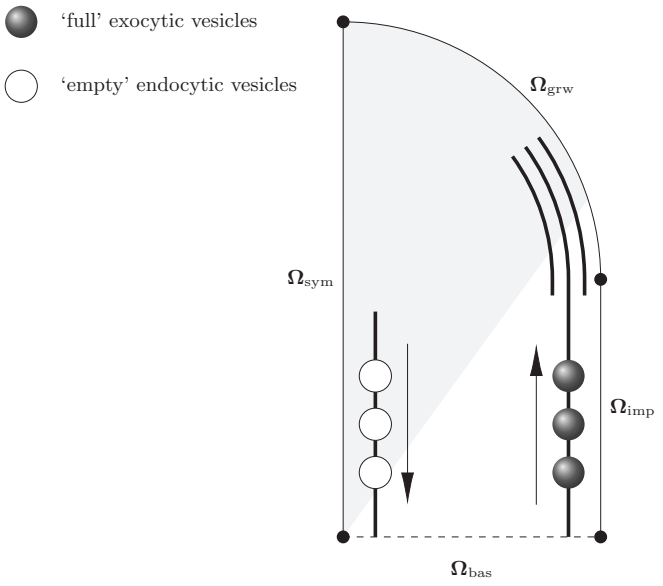

FIG. 7. Suggested mechanism for transport of vesicles in the pollen tube, showing actin bundles (thick interior lines) and dense apical actin fringe running parallel to the peripheral wall, as well as pooling of apical vesicles and shape of the inverted vesicle cone (shaded area). The direction of vesicle movement along actin bundles is given by arrows. The location of each of the four boundaries of the domain is also shown. Image not drawn to scale.

A. Brief overview of the pollen tube

The pollen tube, a cellular protuberance originating from the pollen grain, is a vital component of the fertilization process in plants. Responsible for the delivery of sperm cells from the pollen grain to the ovule, the tube may have to grow over 30 cm in length at speeds in excess of 1 cm h^{-1} [33,34]. This rapid elongation of the tube occurs via tip growth, with expansion localized close to the apical region of the cell [35]. To prevent rupture, new cell membrane and cell wall material must be targeted to the sites of highest expansion. Spherical vesicles in the cytosolic region act as the delivery vectors for this material [18] and are carried by motor myosin proteins along actin filaments in a process referred to as actomyosin transport. These actin filaments, arranged in bundles in the periphery and center of the tube, are oriented in such a way that full peripheral vesicles travel towards the growing apex where they secrete their contents into the wall. In order to maintain the correct ratio of structural components, empty vesicles (comprised mostly of membrane) are also secreted by the wall back into the cytoplasm, where it is hypothesized that they are picked up by myosin on the central actin bundle and travel away from the apex. The combined movement of these vesicles induces a flow in the cytosol, known as cytoplasmic streaming or cyclosis, which further aids in the cycling of vesicles towards and away from the apical region. In this section we show how the method of regularized ringlets can efficiently produce a complete model of cytosolic flow in the pollen tube in a manner deriving directly from physical principles.

B. Mathematical model

1. Geometry and boundary conditions

The typical geometry of the tube (for cylindrical coordinates in the *r*-*z* plane) along with the two vesicle populations and actin bundles can be seen in Fig. 7, in which the static cylindrical shank is joined to a growing apical hemispherical cap. The boundary of the domain is split into four sections: the symmetry boundary $\boldsymbol{\Omega}_{\mathrm{sym}}$ running down the centerline of the tube, the static

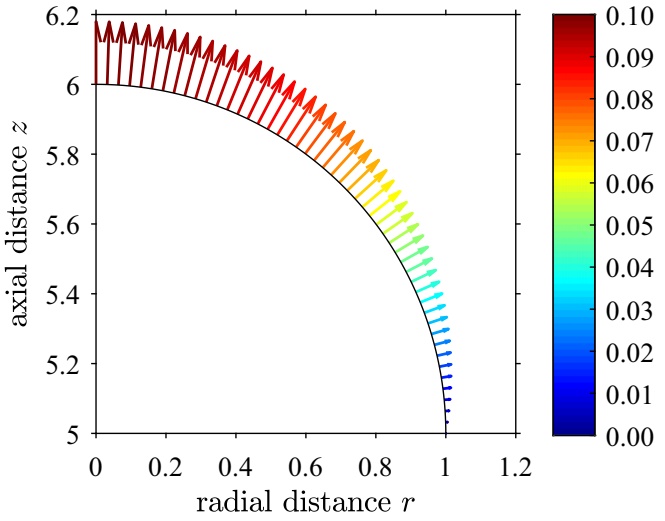

FIG. 8. Growth velocity of the apical boundary, normal to the cell surface and varying from a maximum at the extreme apex to zero at the point where the apical hemisphere joins the adjacent shank. Velocities are scaled by the speed of vesicles on actin (1 μm s^{-1}), with lengths scaled by the radius of the tube (8.13 μm).

impermeable peripheral wall $\mathbf{\Omega}_{\text{imp}}$, the growing apical hemisphere $\mathbf{\Omega}_{\text{grw}}$, and the artificial basal boundary $\mathbf{\Omega}_{\text{bas}}$ (where the computational domain is truncated).

The Reynolds number for fluid flow in the pollen tube can be evaluated using the typical flow speed (approximately 1 μm s^{-1}), tube radius (approximately 8.13 μm), and kinematic viscosity of water (approximately 10^6 μm^2 s^{-1}) to find Re $\approx 10^{-5}$, firmly in the regime of Stokes flow. Although pollen tube growth is typically oscillatory, acceleration and deceleration are small compared to growth speed itself. This enables the use of the steady Stokes equations.

Since the cytosolic flow is induced by the actomyosin transport of vesicles along cytoskeletal actin bundles, forces must be applied inside the computational domain. Singular Stokeslet methods typically do not allow for this unless the surfaces of individual vesicles are discretized, but their small size (approximately 100-nm radius) compared to the typical length scale of the problem and their large number density make this impractical. One solution is to use the method of regularized ringlets instead, placing rings in series along the centerline of the peripheral actin bundle with the parameter ε being used to control the bundle thickness.

The boundary conditions for the fluid velocity $\mathbf{u}$ are given by

$$\begin{aligned} \mathbf{u} &= \mathbf{u}_g \quad \text{on } \mathbf{\Omega}_{\text{grw}}, \\ \mathbf{u} &= \mathbf{0} \quad \text{on } \mathbf{\Omega}_{\text{imp}}, \\ u_r &= \partial u_z/\partial r = 0 \quad \text{on } \mathbf{\Omega}_{\text{sym}}, \end{aligned} \tag{72}$$

in accordance with the assumptions of tip growth and axisymmetry. No restriction is placed on $\mathbf{u}$ on the artificial boundary $\mathbf{\Omega}_{\text{bas}}$. For the growth velocity $\mathbf{u}_g$ in the hemispherical apex, the normal displacement growth assumption of Dumais *et al.* [36] is employed to define

$$\mathbf{u}_g = \mathbf{u}_g(\varphi) := v_g \sin\varphi(\cos\varphi, \sin\varphi), \tag{73}$$

where φ is the angle between the outward-pointing surface normal and the positive r axis (varying from 0 at the point where the hemisphere joins the shank to $\frac{\pi}{2}$ at the extreme apex) and v_g is the growth speed of the tube. An example of how the growth of the boundary varies over the apical hemisphere can be seen in Fig. 8, where the maximum growth speed v_g is equal to 0.1 m s^{-1} and the wall velocity in the adjacent shank (not pictured) is equal to zero.

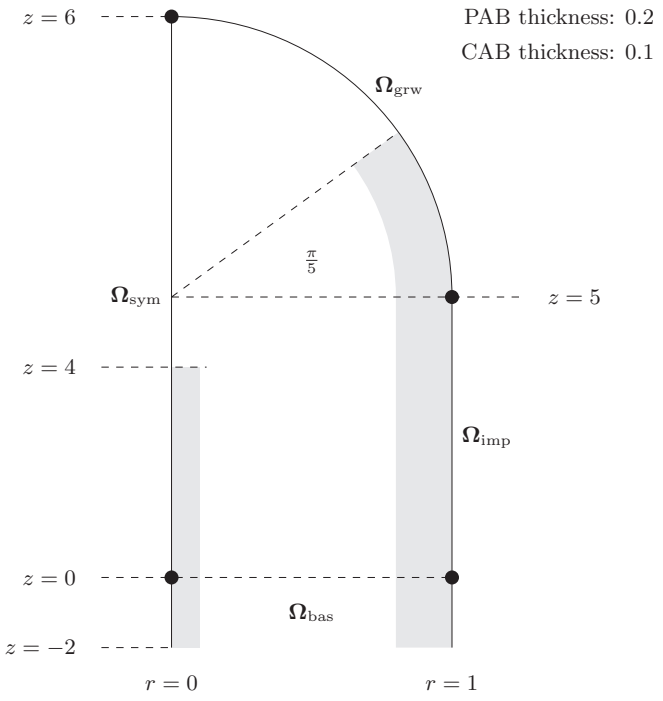

FIG. 9. Geometric elements of the mathematical model for the pollen tube, adapted from the information in Fig. 7. Here PAB and CAB refer to the peripheral actin bundle and central actin bundle, respectively, with the CAB thickness half that of the PAB by axisymmetry. Image not drawn to scale in $\hat{z}$.

2. Actin bundle model

A section of the pollen tube is modeled ranging from the extreme apex to a point equal to six tube radii distal where the domain is artificially truncated. In dimensionless values, the extreme apex is thus given by $(r, z) = (0, 6)$, with $z = 0$ being the distal truncation line. The central line of axisymmetry is given by $r = 0$, with $r = 1$ denoting the peripheral boundary in the shank. The hemispherical apex is the upper-right quarter circle of radius 1, centered at (0,5). The peripheral actin bundle (PAB) is considered adjacent to the pollen tube wall, with its width equal to one-fifth of the pollen tube radius (0.2) and extending at an angle $\varphi = \pi/5$ into the apical hemisphere (see Fig. 9) in accordance with the confocal microscopy imaging of Lovy-Wheeler *et al.* [37]. The central actin bundle (CAB) is located further away from the apex than the PAB and is modeled with a reduced thickness (half that of the PAB) in cylindrical coordinates to account for the central axisymmetry of the tube.

By placing rings of regularized Stokeslets in series along the centerline of the PAB, it is possible to carefully select an appropriate value for the regularization parameter ε such that the region over which the majority of the force distribution is applied is roughly the same as the bundle thickness. The same procedure is employed for the CAB, only with individual regularized Stokeslets rather than ringlets since the centerline coincides with $r = 0$. Using $\varepsilon = 0.05$, it is found that approximately 93% of the total applied force is contained within a region of radius 0.1, which corresponds well to the approximate thickness of the actin bundles. This is shown in Fig. 10, where $\hat{r} = |\mathbf{x}_0 - \mathbf{x}_n|$ and the maximal value of ϕ_ε has been scaled to 1 for the sake of clarity. Smaller values of ε result in an even larger percentage of the total force being contained within $0 \leqslant \hat{r} \leqslant 0.1$ but are increasingly skewed towards $\hat{r} = 0$.

We note that our modeling ignores the presence of a third F-actin structure, the short actin bundles observed in the extreme apex [38]; these bundles are transient and significantly less dense than

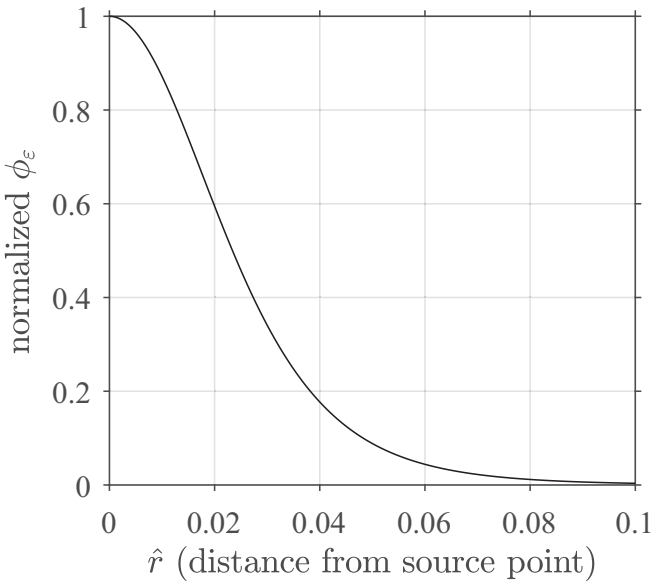

FIG. 10. Controlled spreading of force distribution using ϕ_ε with $\varepsilon = 0.05$.

the thick peripheral and central actin bundles. Further, due to their proximity to the growing tube wall, any effect that these short actin bundles may have on the fluid velocity is likely insignificant compared to the effect of the growth of the wall.

3. Frames of reference

In each of the velocity profiles to be produced, cytosolic velocities are prescribed along the actin bundles in accordance with values taken from the spatiotemporal image correlation spectroscopy (STICS) analysis of Bove *et al.* [33]. This is done under the assumption that the large-scale directed movement of vesicles must be a consequence of cytosolic flow (induced by the smaller-scale movement of individual vesicles along actin). The fluid velocity is defined in terms of two different coordinate systems: the static laboratory frame where $\mathbf{u}_L = (u_r, u_z)$ and the moving tip frame with $\mathbf{u}_T = (u_r, u_z - v_g)$. The laboratory frame represents the fluid velocity relative to a stationary observation point (in which $\mathbf{u}_L \cdot \hat{\mathbf{n}} \neq 0$ on $\mathbf{\Omega}_{\text{grw}}$ due to boundary growth), whereas the tip frame represents the fluid velocity relative to the growing tip (resulting in a static domain with $\mathbf{u}_T \cdot \hat{\mathbf{n}}$ at all boundary points except on $\mathbf{\Omega}_{\text{bas}}$). The steady geometry of the domain for the advancing tip frame means that $\mathbf{u}_T$ satisfies the steady Stokes equations, from which it follows that $\mathbf{u}_L$ is also a solution [since the two differ by the uniform flow field $(0, v_g)$ only].

4. Two model scenarios for comparison

In Sec. IV C 1, we investigate the role of the CAB in vesicle transport. Fluid velocity is prescribed on the PAB only [see Fig. 11(a)] in order to compare the resultant central fluid velocity to experimental results. The centerline of the PAB is modeled using the union of the straight line extending from $(r, z) = (0.9, -2)$ to (0.9,5) and the curve $(r, z) = (0.9\cos\varphi, 5 + 0.9\sin\varphi)$ for $\varphi \in [0, \pi/5]$. The regularized ringlet placement is extended to $z = -2$ to ensure the velocity profile at $z = 0$ is consistent with the rest of the tube. The fluid velocity on the straight line is given by $(u_r, u_z) = (0, 0.5)$ with the fluid velocity on the curve being tangential and of constant magnitude, that is, $(u_r, u_z) = 0.5(\sin\varphi, \cos\varphi)$ for $\varphi \in [0, \pi/5]$. On the peripheral wall (again extended to $z = -2$), the velocity is $\mathbf{0}$ in the shank and prescribed according to the growth speed v_g of the tube in the apical hemisphere using the velocity function $\mathbf{u}_g(\varphi) = v_g \sin\varphi(\cos\varphi, \sin\varphi)$ for $\varphi \in [0, \pi/2]$.

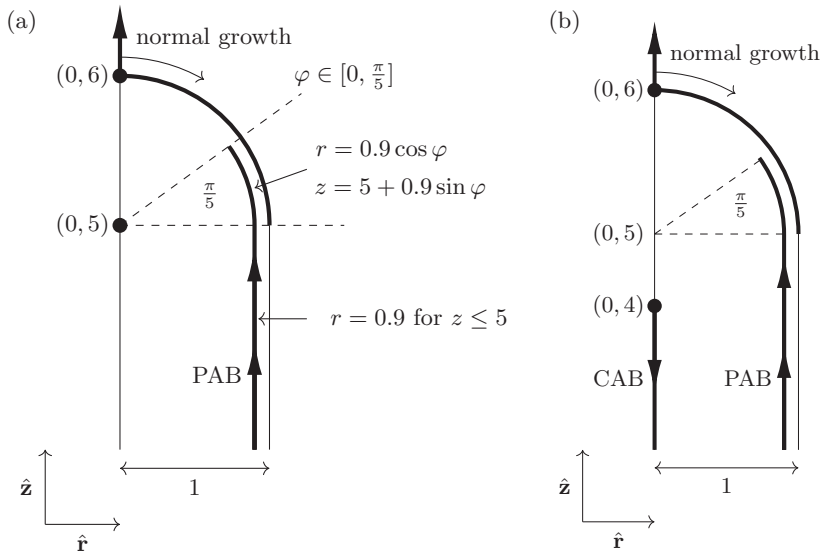

FIG. 11. Dimensionless schematic diagrams for situations considered in (a) Sec. IV C 1 and (b) Sec. IV C 2. Thick lines denote locations on which velocity is prescribed in each case.

In Sec. IV C 2, the velocity of the growing boundary is varied in order to determine the effect of the growth speed of the tube on the cytosolic velocity. Fluid velocity is prescribed on each of the PAB, the CAB, and the growing boundary accordingly [see Fig. 11(b)]. Fluid velocity along the PAB is kept constant at 0.5 μm s^{-1} based on the observation that cytoplasmic streaming rates are typically independent of pollen tube growth rates [39]. The fluid velocity on the centerline of the central actin bundle, given by $r = 0$ for $-2 \leqslant z \leqslant 4$, is also prescribed. It is assumed that vesicles are sufficiently closely packed on this bundle that the fluid velocity at its center can be approximated by the speed of vesicles on actin (1 μm s^{-1}), giving $(u_r, u_z) = (0, -1)$. Since these node locations are at $r = 0$, standard regularized Stokeslets must be used here.

A regularization parameter of $\varepsilon = 0.05$ is chosen in all cases and the ringlets are linearly spaced a distance approximately 0.025 apart, resulting in a smooth velocity profile. The flow velocity for $z < 3$ (not pictured) always matches the flow velocity at $z = 3$ almost exactly, with no further change occurring in the $\hat{\mathbf{z}}$ direction.

C. Results

1. Role of the central actin bundle

The CAB has long been hypothesized to aid in the removal of vesicles from the apical region, but direct observation of vesicle transport along actin is often hindered by the small size of vesicles (typically below the resolution limit of conventional confocal microscopes). Higher resolution imaging methods such as evanescent wave microscopy have been used to observe long-range vesicle movement (presumably a result of actomyosin transport) in the periphery of the tube [40], but the limited penetration depths available in these methods (less than or equal to 400 nm) do not allow for imaging of the central region. Spatiotemporal image correlation spectroscopy analysis suggests a way of determining whether the central bundle participates in vesicle transport. Directed vesicle movement in the periphery of the tube is not seen to exceed speeds of approximately 0.5 μm s^{-1}, smaller than the approximately 0.8 μm s^{-1} observed in the center [33]. By using the method of regularized ringlets and prescribing fluid velocity only along the PAB, where $|\mathbf{u}_T| = 0.5$ μm s^{-1} and the tube boundary with apical growth speed $v_g = 0.1$ μm s^{-1}, the resulting fluid velocity in the

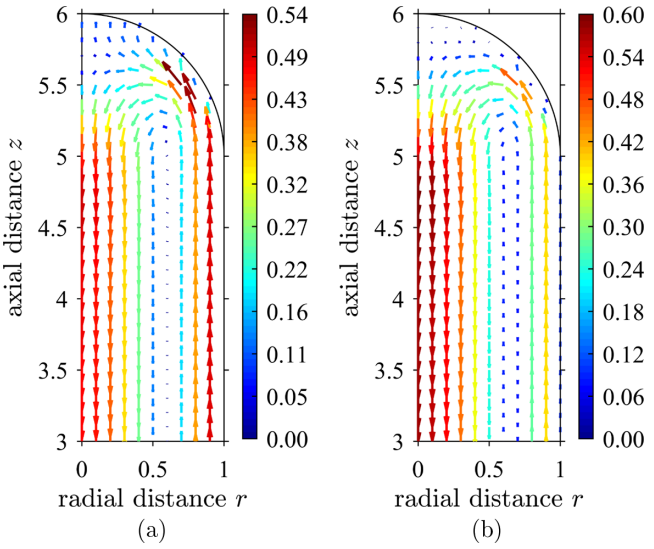

FIG. 12. Dimensionless magnitude and direction of apical cytosolic flow in (a) the laboratory frame and (b) the tip frame, calculated using the prescribed velocity of magnitude 0.5 μm s^{-1} on the peripheral actin bundle, as well as a prescribed normal velocity with maximum magnitude equal to the growth speed 0.1 μm s^{-1} at the apical boundary. Velocities are scaled by the speed of vesicles on actin (1 μm s^{-1}), with lengths scaled by the radius of the tube (8.13 μm).

center should provide further insight insight into whether the central bundle participates in vesicle transport.

The results of this investigation can be seen in Fig. 12, with both laboratory [Fig. 12(a)] and tip [Fig. 12(b)] frames shown. The shape of the velocity profile in Fig. 12(a) is in excellent agreement with the STICS analysis of Bove *et al.* [33], with a wider band of basal flow through the center than apical flow in the periphery. However, despite an arguably exaggerated prescribed peripheral fluid velocity of 0.5 μm s^{-1}, fluid velocity in the center does not achieve speeds of 0.8 μm s^{-1}. This is a strong indication that the CAB must also participate in the transport of vesicles, particularly considering that that our current implementation of the Stokes equations does not account for variations in local fluid viscosity (known to be larger in the presence of filamentous actin networks [41], reducing the fluid velocity induced by any given force). The increased flow speed through the center of the tube can be easily accounted for by inclusion of additional drag from actomyosin vesicle transport (known to reach speeds of up to 2 μm s^{-1} [39,42]) along the CAB, with the largest velocities being observed at the very center as a result of the reduced cytosolic volume in this region.

2. Influence of growth speed

We now turn our attention to the effect of tube growth speed on the cytosolic velocity profile. Three additional velocity profiles are produced, based on three different growth speeds for the tube (0, 0.1, and 0.2 μm s^{-1}). These speeds (approximately) correspond to that of a static tube, the typical growth rate cited in Bove *et al.* [33], and the average growth rate measured by Vidali *et al.* [39] for the *Lilium longiflorum* species. Fluid velocity is prescribed along the PAB ($|\mathbf{u}_T| = 0.5$ μm s^{-1}), the CAB ($u_z = -1$ μm s^{-1}), and the tube boundary ($v_g = 0, 0.1, 0.2$ μm s^{-1}), in each case.

Figures 13(a)–13(c) show the velocity profiles for each of these three tube growth speeds in the laboratory frame. Significant differences can be seen between the three profiles, in both the magnitude and direction of the fluid velocity. In particular, at larger growth speeds there is a wider band of cytosolic flow in the positive $\hat{\mathbf{z}}$ direction in the peripheral region and the central band of

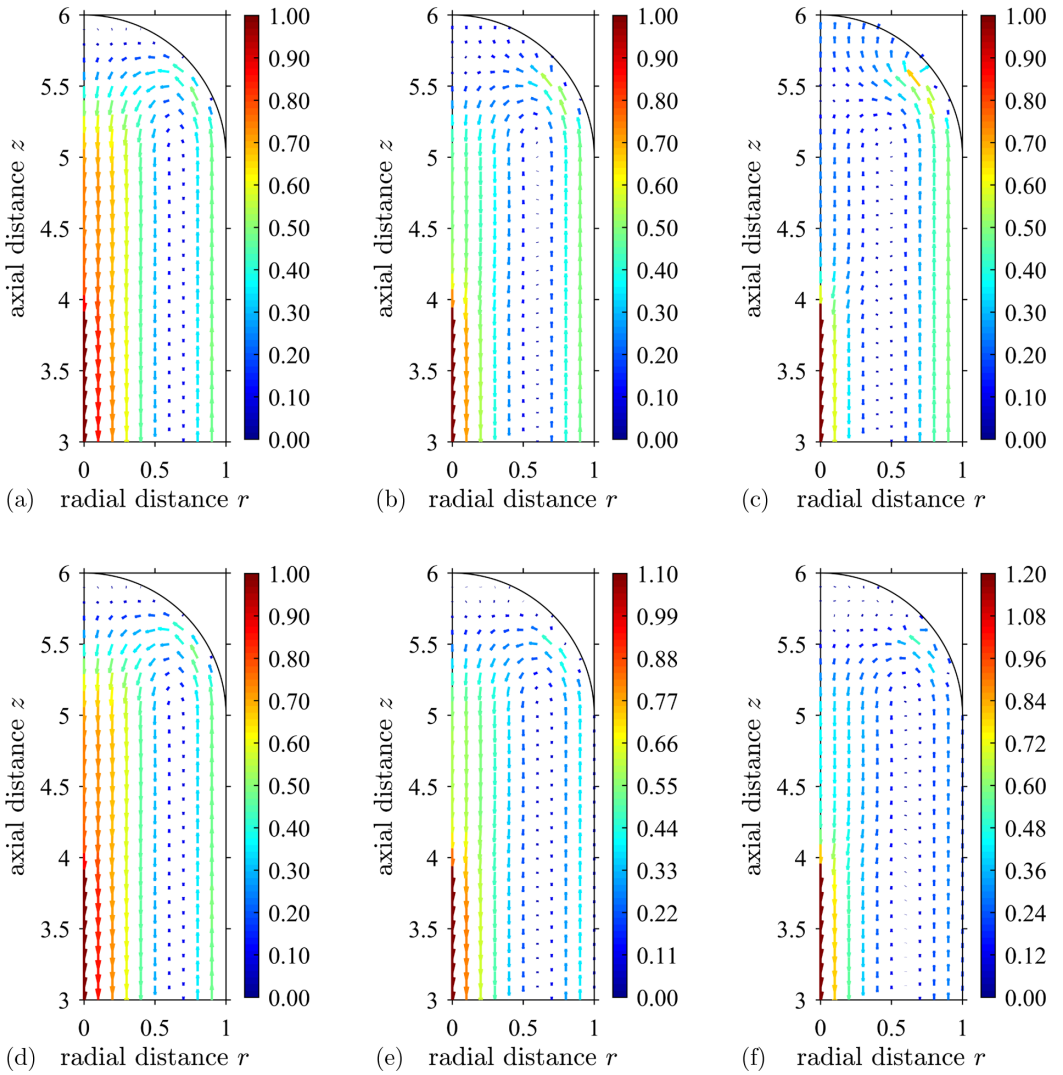

FIG. 13. Dimensionless magnitude and direction of apical cytosolic flow in (a)–(c) the laboratory frame and (d)–(f) the tip frame, calculated using prescribed velocities of magnitude 0.5 and 1 $\mu\mathrm{m\,s^{-1}}$ on the peripheral and central actin bundles, respectively, as well as a prescribed normal velocity with maximum magnitude equal to the growth speed (a) and (d) 0 $\mu\mathrm{m\,s^{-1}}$, (b) and (e) 0.1 $\mu\mathrm{m\,s^{-1}}$, and (c) and (f) 0.2 $\mu\mathrm{m\,s^{-1}}$, at the apical boundary. Velocities are scaled by the speed of vesicles on actin (1 $\mu\mathrm{m\,s^{-1}}$), with lengths scaled by the radius of the tube (8.13 μm).

basal flow is both narrower and of a reduced magnitude. This is an expected consequence of mass conservation, since in a tube with a faster growth speed more fluid must flow towards the apical region to fill the increasing space.

Figures 13(d)–13(f) show the velocity profiles for each of these three tube growth speeds in the tip frame. Here the growth speed of the tube has been subtracted from the $\hat{\mathbf{z}}$ component of the fluid velocity for each corresponding velocity profile in the laboratory frame. Interestingly, the differences between the velocity profiles are significantly less pronounced in this frame of reference. Differences in the magnitude of the fluid velocity still persist, but the overall shapes of the profiles bear a striking similarity. The persistent shape of the velocity profiles seen in Figs. 13(d)–13(f) could

help explain the observed similarities in the distribution of the apical vesicle population and other elements of the cytoplasm across multiple pollen tube species and throughout different phases of oscillatory growth.

V. CONCLUSIONS AND FUTURE WORK

In this paper, the regularized fundamental solution for the velocity (single-layer potential) and stress (double-layer potential) due to an axisymmetric ring of smoothed point forces (the regularized ringlet) was derived, expanding on the work of Cortez *et al.* [11,12]. The velocity solution, written in the form of complete elliptic integrals of the first and second kind, tends to the singular solution of Pozrikidis [19] in the limit as the regularization parameter ε tends to zero.

For the resistance problem on the translating and rotating unit sphere, the method of regularized ringlets was shown to produce small relative errors in drag calculations and small condition numbers for the underlying resistance matrices. Further testing in the case of the translating unit sphere shows that the regularized ringlet performs favorably compared to the traditional method of regularized Stokeslets in terms of both accuracy (Appendix E) and speed (Appendix G) and that it possesses more satisfactory convergence properties than the singular ringlet (Appendix F).

The applicability of the regularized ringlet to fluid flow problems involving body surface motion in the $\hat{\mathbf{r}}$ direction (perpendicular to the line of axisymmetry) was established in the example of Purcell's toroidal swimmer. Using the regularized ringlet method, we were able to reproduce Leshansky and Kenneth's [20] results for the scaled propulsion velocity of the toroidal swimmer, propelled by surface tank treading against the direction of motion of its outer surface. Our results show a significant improvement over the asymptotic solution found by integrating a centerline distribution of rotlets in the limit as slenderness decreases ($s_0 \to 0$). The use of regularized ringlets also yields the drag force at all points on the torus surface for the toroidal swimmer, information that is not readily available using the series or rotlet solutions.

One limitation of the method derived in this paper concerns applicability to multibody Stokes flow problems, in which regularized ringlets can only be employed if the motion of all bodies is restricted to a single line of axisymmetry. When this is not the case, the resulting nonconstant force distribution around the central line of axisymmetry of each individual body means that analytical ringlet evaluation is not possible. The method could not, for example, be employed to model the interactions between multiple swimming tori for all of the cases considered in a recent paper by Huang and Fauci [43] (in which the standard method of regularized Stokeslets is used). We do note however that Huang and Fauci's optimal configuration for toroidal swimmers (in terms of translational velocity and energy efficiency) consists of a corotating pair with a common line of axisymmetry, a situation that regularized ringlets can model very effectively. The effectiveness of the method of regularized ringlets in modeling this corotating toroidal pair, suggested as a potential design for motile nanomachines [43], highlights the possible future usage of the method in the modeling of other efficient forms of axisymmetric motion.

In order to elucidate the further benefits of regularization, we studied the case of cytosolic flow in the growing pollen tube. Here the inducing drag force is the result of the directed actomyosin transport of vesicles inside the fluid, making application of singular Stokeslet methods particularly challenging. Since the area over which the force is applied is also relatively large (and somewhat indeterminate), being able to use the regularization parameter ε to control the spreading of the force is also vital to the solution.

Using the regularized ringlet solution for the steady Stokes equations, we were able to show that it is highly likely that the central actin bundle plays a role in the removal of vesicles from the apical pool. This has long been hypothesized, with vesicle movement through the central region seen to reach speeds of up to 2 $\mu\mathrm{m\,s^{-1}}$ [33] (similar to those of actomyosin transport), but direct evidence has been lacking. Fluid velocity profiles based on drag induced by actomyosin transport of vesicles along the peripheral bundle alone show that cytosolic flow in the central region does not reach these speeds, strongly suggesting that actomyosin transport takes place on the central actin bundle.

During further investigation, we were able to show that the shape of the cytosolic velocity profile relative to the moving tip is largely independent of the growth speed of the tube (under the assumption that the actin profile is able to keep up with the advancing tip). This provides some insight into how the tube is able to consistently orient its internal architecture across multiple pollen tube species and in spite of changes in growth speed during different phases of oscillatory growth. Future work on the pollen tube can be done by using the cytosolic velocity profiles we have produced in tandem with an advection-diffusion-reaction equation for the spatiotemporal distribution of vesicles in the pollen tube. Investigating the conditions necessary to produce the inverted vesicle cone almost universally observed in the apex of the angiosperm pollen tube yields results concerning the appropriate values for different parameters pertaining to tube growth. We believe that the regularized Stokeslet ring method will be of benefit to further studies in the fluid dynamics of axisymmetric growth and beyond.

ACKNOWLEDGMENTS

The authors acknowledge funding from the Engineering and Physical Sciences Research Council in the form of a Doctoral Training Award through Grant No. EP/M508202/1 to J.T. and Grants No. EP/N021096/1 to D.J.S. and No. EP/M00015X/1 to R.J.D.). The authors would also like to thank Professor Anja Geitmann and Dr. Youssef Chebli (both of the Department of Plant Science, Faculty of Agriculture and Environmental Sciences, McGill University, Sainte-Anne-de-Bellevue, Canada) for their valuable insights on pollen tube physiology and growth.

APPENDIX A: REGULARIZED STOKESLETS IN CYLINDRICAL COORDINATES FOR RINGLET EVALUATION

The expressions $S_{ij}^{\varepsilon}(\mathbf{x}_0, \mathbf{x})$ for the fluid point $\mathbf{x}_0 = (r_0, 0, z_0)$ and ring point $\mathbf{x}_n = (r_n, \theta, z_n)$ in cylindrical coordinates are

$$
\begin{aligned}
S_{11}^{\varepsilon} &= \frac{1}{\hat{r}_{\varepsilon}^3}[2(r_0 - r_n\cos\theta)^2 + (r_n\sin\theta)^2 + (z_0 - z_n)^2 + 2\varepsilon^2],\\
S_{12}^{\varepsilon} &= \frac{1}{\hat{r}_{\varepsilon}^3}[-(r_0 - r_n\cos\theta)(r_n\sin\theta)],\\
S_{13}^{\varepsilon} &= \frac{1}{\hat{r}_{\varepsilon}^3}[(r_0 - r_n\cos\theta)(z_0 - z_n)],\\
S_{21}^{\varepsilon} &= \frac{1}{\hat{r}_{\varepsilon}^3}[-(r_0 - r_n\cos\theta)(r_n\sin\theta)],\\
S_{22}^{\varepsilon} &= \frac{1}{\hat{r}_{\varepsilon}^3}[(r_0 - r_n\cos\theta)^2 + 2(r_n\sin\theta)^2 + (z_0 - z_n)^2 + 2\varepsilon^2],\\
S_{23}^{\varepsilon} &= \frac{1}{\hat{r}_{\varepsilon}^3}[-(r_n\sin\theta)(z_0 - z_n)],\\
S_{31}^{\varepsilon} &= \frac{1}{\hat{r}_{\varepsilon}^3}[(r_0 - r_n\cos\theta)(z_0 - z_n)],\\
S_{32}^{\varepsilon} &= \frac{1}{\hat{r}_{\varepsilon}^3}[-(r_n\sin\theta)(z_0 - z_n)],\\
S_{33}^{\varepsilon} &= \frac{1}{\hat{r}_{\varepsilon}^3}[(r_0 - r_n\cos\theta)^2 + (r_n\sin\theta)^2 + 2(z_0 - z_n)^2 + 2\varepsilon^2],
\end{aligned}
\tag{A1}
$$

in which $\hat{r}_{\varepsilon} = [(r_0 - r_n\cos\theta)^2 + (r_n\sin\theta)^2 + (z_0 - z_n)^2 + \varepsilon^2]^{1/2}$.

APPENDIX B: EVALUATING THE LIMITING BEHAVIOR OF $R^{\varepsilon}_{\alpha\beta}$

To understand the behavior of $R^{\varepsilon}_{\alpha\beta}$ as $r_n, r_0 \to 0$, it is easiest to consider $R^{\varepsilon}_{\alpha\beta}$ in the form

$$R^{\varepsilon}_{rr}(\mathbf{x}_0, \mathbf{x}_n) = r_n\{-r_0 r_n I_0 + [2\tau - (z_0 - z_n)^2]I_1 - 3r_0 r_n I_2\}, \tag{B1}$$

$$R^{\varepsilon}_{rz}(\mathbf{x}_0, \mathbf{x}_n) = r_n(z_0 - z_n)(r_0 I_0 - r_n I_1), \tag{B2}$$

$$R^{\varepsilon}_{zr}(\mathbf{x}_0, \mathbf{x}_n) = r_n(z_0 - z_n)(-r_n I_0 + r_0 I_1), \tag{B3}$$

$$R^{\varepsilon}_{zz}(\mathbf{x}_0, \mathbf{x}_n) = r_n\{[\tau + (z_0 - z_n)^2 + \varepsilon^2]I_0 - 2r_0 r_n I_1\}, \tag{B4}$$

$$R^{\varepsilon}_{\theta\theta}(\mathbf{x}_0, \mathbf{x}_n) = r_n[r_0 r_n I_0 + (\tau + \varepsilon^2)I_1 - 3r_0 r_n I_2], \tag{B5}$$

in which

$$I_0 = \frac{4k^3}{(4r_0 r_n)^{3/2}}\left(\frac{1}{1-k^2}E\right), \tag{B6}$$

$$I_1 = \frac{4k^3}{(4r_0 r_n)^{3/2}}\left(\frac{2-k^2}{k^2(1-k^2)}E - \frac{2}{k^2}F\right), \tag{B7}$$

$$I_2 = \frac{4k^3}{(4r_0 r_n)^{3/2}}\left(\frac{k^4 - 8k^2 + 8}{k^4(1-k^2)}E - \frac{4(2-k^2)}{k^4}F\right), \tag{B8}$$

with $\tau = r_0^2 + r_n^2 + (z_0 - z_n)^2 + \varepsilon^2$ and $k^2 := 4r_0 r_n/(\tau + 2r_0 r_n)$. Evaluating $\lim_{k\to 0} I_n$ for each $n \in \{0, 1, 2\}$ and substituting these into Eqs. (B1)–(B5) yields the desired results for $\lim_{r_n\to 0} R^{\varepsilon}_{\alpha\beta}$ and $\lim_{r_0\to 0} R^{\varepsilon}_{\alpha\beta}$.

The first step in evaluating these limits is to observe that from the definition of k, it follows that $k \to 0$ as either $r_0 \to 0$ or $r_n \to 0$ (or both). Further, noting that

$$\lim_{k\to 0}\frac{4k^3}{(4r_0 r_n)^{3/2}} = \lim_{k\to 0}\frac{4\left(\frac{4r_0 r_n}{\tau + 2r_0 r_n}\right)^{3/2}}{(4r_0 r_n)^{3/2}} = \frac{4}{\tau^{3/2}}, \tag{B9}$$

in which the value of τ as $k \to 0$ depends on whether $r_0 \to 0$ or $r_n \to 0$ (or both), it is observed that I_0, I_1, and I_2 contain a common finite term outside of the large parentheses. Evaluating the remaining parts of I_0, I_1, and I_2 in the limit as $k \to 0$ requires employing the power series expansions of the complete elliptic integrals [23] such that

$$F(k) = \frac{\pi}{2}\left(1 + \frac{1}{4}k^2 + \frac{9}{64}k^4 + \cdots\right), \tag{B10}$$

$$E(k) = \frac{\pi}{2}\left(1 - \frac{1}{4}k^2 - \frac{9}{64}k^4 + \cdots\right). \tag{B11}$$

Letting $E \sim \pi/2$, it follows that

$$\lim_{k\to 0}\left(\frac{1}{1-k^2}E\right) = \frac{\pi}{2}. \tag{B12}$$

Similarly, letting $E \sim \frac{\pi}{2}(1 - \frac{1}{4}k^2)$ and $F \sim \frac{\pi}{2}(1 + \frac{1}{4}k^2)$, it can be found that

$$\lim_{k\to 0}\left(\frac{2-k^2}{k^2(1-k^2)}E - \frac{2}{k^2}F\right) = 0. \tag{B13}$$

Finally, using $E \sim \frac{\pi}{2}(1 - \frac{1}{4}k^2 - \frac{9}{64}k^4)$ and $F \sim \frac{\pi}{2}(1 + \frac{1}{4}k^2 + \frac{9}{64}k^4)$ yields

$$\lim_{k\to 0}\left(\frac{k^4 - 8k^2 + 8}{k^4(1-k^2)}E - \frac{4(2-k^2)}{k^4}F\right) = -\frac{\pi}{8}. \tag{B14}$$

Compiling all of the above gives

$$I_0 \to 2\pi/\tau^{3/2}, \quad I_1 \to 0, \quad I_2 \to -\pi/2\tau^{3/2} \quad \text{as } k \to 0, \tag{B15}$$

which upon substitution into the expressions for $R^{\varepsilon}_{\alpha\beta}$ yields

$$\lim_{r_n\to 0} R^{\varepsilon}_{\alpha\beta} \equiv 0, \tag{B16}$$

$$\lim_{r_0\to 0} R^{\varepsilon}_{rr} = \lim_{r_0\to 0} R^{\varepsilon}_{rz} = \lim_{r_0\to 0} R^{\varepsilon}_{\theta\theta} = 0, \tag{B17}$$

$$\lim_{r_0\to 0} R^{\varepsilon}_{zr} = -2\pi r_n^2(z_0 - z_n)/\tau^{3/2}, \tag{B18}$$

$$\lim_{r_0\to 0} R^{\varepsilon}_{zz} = 2\pi r_n(\tau + (z_0 - z_n)^2 + \varepsilon^2)/\tau^{3/2}. \tag{B19}$$

APPENDIX C: FLUID FLOW INDUCED BY UNIT RINGLET FORCES

Figure 14 shows the fluid velocity induced by a ringlet located at $(r, z) = (0.5, 0.5)$ with associated unit force in the $\hat{\mathbf{r}}$ and $\hat{\mathbf{z}}$ directions, both under free-space conditions [Figs. 14(a) and 14(c)] and in the presence of a cylindrical wall at $r = 1$ [Figs. 14(b) and 14(d)], with the wall also represented by Stokes ringlets. In the presence of the bounding wall, closed streamlines and toroidal eddies are observed.

APPENDIX D: EVALUATING THE DOUBLE-LAYER POTENTIAL

Recall the form of the double-layer potential

$$(\mathrm{DLP})_i = \frac{1}{8\pi}\int_{\partial D} u_j(\mathbf{x}) T^{\varepsilon}_{ijk}(\mathbf{x}_0, \mathbf{x}) n_k(\mathbf{x}) dS(\mathbf{x}), \tag{D1}$$

in which the stress tensor T^{ε}_{ijk} is given by

$$\begin{aligned} T^{\varepsilon}_{ijk}(\mathbf{x}_0, \mathbf{x}) = &-6\frac{(x_{0,i} - x_i)(x_{0,j} - x_j)(x_{0,k} - x_k)}{(|\mathbf{x}_0 - \mathbf{x}|^2 + \varepsilon^2)^{5/2}} \\ &- 3\varepsilon^2\frac{(x_{0,i} - x_i)\delta_{jk} + (x_{0,j} - x_j)\delta_{ik} + (x_{0,k} - x_k)\delta_{ij}}{(|\mathbf{x}_0 - \mathbf{x}|^2 + \varepsilon^2)^{5/2}}. \end{aligned} \tag{D2}$$

As with the Stokeslet S^{ε}_{ij} in the single-layer potential, the stress tensor T^{ε}_{ijk} can be expressed in cylindrical coordinates via

$$x_{0,1} - x_1 = r_0 - r_n\cos\theta, \tag{D3}$$

$$x_{0,2} - x_2 = -r_n\sin\theta, \tag{D4}$$

$$x_{0,3} - x_3 = z_0 - z_n, \tag{D5}$$

$$|\mathbf{x}_0 - \mathbf{x}|^2 = (r_0 - r_n\cos\theta)^2 + (r_n\sin\theta)^2 + (z_0 - z_n)^2 \tag{D6}$$

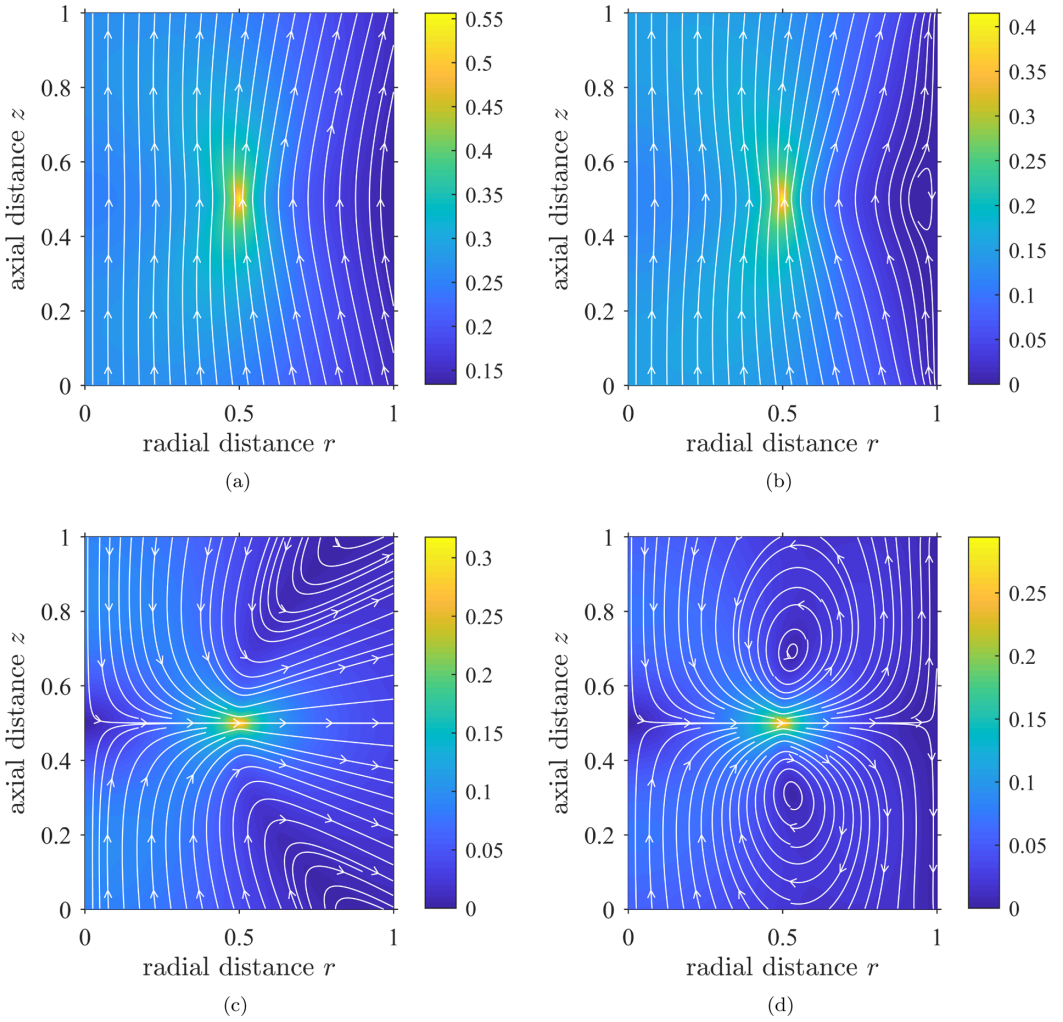

FIG. 14. Fluid flow induced by unit force on ringlet placed at $(r, z) = (0.5, 0.5)$. (a) and (b) show axial force, with (c) and (d) showing radial force. A no-slip bounding wall is present at $r = 1$ in cases (b) and (d).

and the Cartesian and cylindrical forms of the flow vector $\mathbf{u}$ are related via $u_j = \Theta_{j\beta} u_\beta$ in which

$$\Theta(\theta) = \begin{pmatrix} \cos\theta & -\sin\theta & 0 \\ \sin\theta & \cos\theta & 0 \\ 0 & 0 & 1 \end{pmatrix}. \tag{D7}$$

Recalling that the azimuthal component of the normal to an axisymmetric body is zero, the transformation from polar to Cartesian coordinates is $n_i = \Psi_{i\alpha} n_\alpha$, where

$$\Psi(\theta) = \begin{pmatrix} \cos\theta & 0 & 0 \\ \sin\theta & 0 & 0 \\ 0 & 0 & 1 \end{pmatrix}. \tag{D8}$$

Let

$$Q_{\alpha\beta\gamma} = r\delta_{\alpha i} \int_0^{2\pi} \Theta_{j\beta} T^{\varepsilon}_{ijk} \Psi_{k\gamma} d\theta \tag{D9}$$

such that

$$(\mathrm{DLP})_\alpha = \frac{1}{8\pi}\int_0^L Q_{\alpha\beta\gamma}u_\beta n_\gamma ds. \tag{D10}$$

For fixed α, nonzero elements of $Q_{\alpha\beta\gamma}$ are given by

$$\begin{aligned}
Q_{\alpha 11} &= r_n\delta_{\alpha i}\int_0^{2\pi}\left(T^\varepsilon_{i11}\cos^2\theta + T^\varepsilon_{i12}\sin\theta\cos\theta + T^\varepsilon_{i21}\sin\theta\cos\theta + T^\varepsilon_{i22}\sin^2\theta\right)d\theta,\\
Q_{\alpha 13} &= r_n\delta_{\alpha i}\int_0^{2\pi}\left(T^\varepsilon_{i13}\cos\theta + T^\varepsilon_{i23}\sin\theta\right)d\theta,\\
Q_{\alpha 21} &= r_n\delta_{\alpha i}\int_0^{2\pi}\left(-T^\varepsilon_{i11}\sin\theta\cos\theta - T^\varepsilon_{i12}\sin^2\theta + T^\varepsilon_{i21}\cos^2\theta + T^\varepsilon_{i22}\sin\theta\cos\theta\right)d\theta,\\
Q_{\alpha 23} &= r_n\delta_{\alpha i}\int_0^{2\pi}\left(-T^\varepsilon_{i13}\sin\theta + T^\varepsilon_{i23}\cos\theta\right)d\theta,\\
Q_{\alpha 31} &= r_n\delta_{\alpha i}\int_0^{2\pi}\left(T^\varepsilon_{i31}\cos\theta + T^\varepsilon_{i32}\sin\theta\right)d\theta,\\
Q_{\alpha 33} &= r_n\delta_{\alpha i}\int_0^{2\pi}\left(T^\varepsilon_{i33}\right)d\theta
\end{aligned} \tag{D11}$$

such that each $Q_{\alpha\beta\gamma}$ is a linear sum of terms of the form

$$\langle\!\langle \bullet \rangle\!\rangle_{ijk} := r_n\int_0^{2\pi} T^\varepsilon_{ijk}\bullet\, d\theta. \tag{D12}$$

Letting

$$J_{m,n} := r_n\int_0^{2\pi}\frac{\sin^m\theta\cos^n\theta}{(\tau - 2r_0r_n\cos\theta)^{5/2}}\,d\theta, \tag{D13}$$

in which $J_{m,n} = 0$ for m odd, each of the necessary $\langle\!\langle\bullet\rangle\!\rangle_{ijk}$ can be written as

$$\begin{aligned}
\langle\!\langle\cos^2\theta\rangle\!\rangle_{111} &= -\left(6r_0^3 + 9\varepsilon^2r_0\right)J_{0,2} + \left(18r_0^2r_n + 9\varepsilon^2r_n\right)J_{0,3} - 18r_0r_n^2J_{0,4} + 6r_n^3J_{0,5},\\
\langle\!\langle\sin\theta\cos\theta\rangle\!\rangle_{112} &= \left(3\varepsilon^2r_n + 6r_0^2r_n\right)J_{2,1} - 12r_0r_n^2J_{2,2} + 6r_n^3J_{2,3},\\
\langle\!\langle\sin^2\theta\rangle\!\rangle_{122} &= -3\varepsilon^2r_0J_{2,0} + 3\varepsilon^2r_nJ_{2,1} - 6r_0r_n^2J_{4,0} + 6r_n^3J_{4,1},\\
\langle\!\langle\cos\theta\rangle\!\rangle_{113} &= -3(z_0 - z_n)\left[\left(2r_0^2 + \varepsilon^2\right)J_{0,1} - 4r_0r_nJ_{0,2} + 2r_n^2J_{0,3}\right],\\
\langle\!\langle\sin\theta\rangle\!\rangle_{123} &= 6r_n(z_0 - z_n)(r_0J_{2,0} - r_nJ_{2,1}),\\
\langle\!\langle 1\rangle\!\rangle_{133} &= [6(z_0 - z_n)^2 + 3\varepsilon^2](-r_0J_{0,0} + r_nJ_{0,1});\\
\langle\!\langle\sin\theta\cos\theta\rangle\!\rangle_{211} &= \left(3\varepsilon^2r_n + 6r_0^2r_n\right)J_{2,1} - 12r_0r_n^2J_{2,2} + 6r_n^3J_{2,3},\\
\langle\!\langle\sin^2\theta\rangle\!\rangle_{212} &= -3\varepsilon^2r_0J_{2,0} + 3\varepsilon^2r_nJ_{2,1} - 6r_0r_n^2J_{4,0} + 6r_n^3J_{4,1},\\
\langle\!\langle\cos^2\theta\rangle\!\rangle_{221} &= -3\varepsilon^2r_0J_{0,2} + 3\varepsilon^2r_nJ_{0,3} + 6r_n^3J_{2,3} - 6r_0r_n^2J_{2,2},\\
\langle\!\langle\sin\theta\cos\theta\rangle\!\rangle_{222} &= 9\varepsilon^2r_nJ_{2,1} + 6r_n^3J_{4,1},\\
\langle\!\langle\sin\theta\rangle\!\rangle_{213} &= 6r_n(z_0 - z_n)(r_0J_{2,0} - r_nJ_{2,1}),\\
\langle\!\langle\cos\theta\rangle\!\rangle_{223} &= -3\varepsilon^2(z_0 - z_n)J_{0,1} - 6r_n^2(z_0 - z_n)J_{2,1};\\
\langle\!\langle\cos^2\theta\rangle\!\rangle_{311} &= -3(z_0 - z_n)\left[\left(2r_0^2 + \varepsilon^2\right)J_{0,2} - 4r_0r_nJ_{0,3} + 2r_n^2J_{0,4}\right],
\end{aligned}$$

$$\begin{aligned}
\langle\langle \sin\theta\cos\theta\rangle\rangle_{312} &= 6r_0r_n(z_0-z_n)J_{2,1} - 6r_n^2(z_0-z_n)J_{2,2},\\
\langle\langle \sin^2\theta\rangle\rangle_{322} &= -3\varepsilon^2(z_0-z_n)J_{2,0} - 6r_n^2(z_0-z_n)J_{4,0},\\
\langle\langle \cos\theta\rangle\rangle_{313} &= [6(z_0-z_n)^2 + 3\varepsilon^2](-r_0J_{0,1} + r_nJ_{0,2}),\\
\langle\langle \sin\theta\rangle\rangle_{323} &= [6r_n(z_0-z_n)^2 + 3r_n\varepsilon^2]J_{2,0},\\
\langle\langle 1\rangle\rangle_{333} &= -[6(z_0-z_n)^3 + 9\varepsilon^2(z_0-z_n)]J_{0,0}.
\end{aligned} \tag{D14}$$

Using the double-angle formulas for sin and cos, we are able to express $J_{m,n}$ purely in terms of even powers of cos such that

$$J_{m,n} = \lambda(2^m)\int_0^{\pi/2} \frac{(2\cos^2\theta - 1)^n(1-\cos^2\theta)^{m/2}\cos^m\theta}{(1-k^2\cos^2\theta)^{5/2}}\,d\theta \quad \text{for } m \text{ even}, \tag{D15}$$

where $\lambda = r_n(k/\sqrt{r_0r_n})^5/8 = 4r_n(\sqrt{\tau + 2r_0r_n})^{-5}$. Note that the upper limit of integration was first reduced by application of the double-angle formulas, followed by the even parity of the resulting integrand about $\pi/2$. If we further define

$$C_m = \lambda\int_0^{\pi/2} \frac{\cos^{2m}\theta}{(1-k^2\cos^2\theta)^{5/2}}d\theta,$$

then expanding Eq. (D15) for the relevant values of m and n yields

$$\begin{aligned}
J_{0,0} &= +C_0,\\
J_{0,1} &= -C_0 + 2C_1,\\
J_{0,2} &= +C_0 - 4C_1 + 4C_2,\\
J_{0,3} &= -C_0 + 6C_1 - 12C_2 + 8C_3,\\
J_{0,4} &= +C_0 - 8C_1 + 24C_2 - 32C_3 + 16C_4,\\
J_{0,5} &= -C_0 + 10C_1 - 40C_2 + 80C_3 - 80C_4 + 32C_5;\\
J_{2,0} &= 4(+C_1 - C_2),\\
J_{2,1} &= 4(-C_1 + 3C_2 - 2C_3),\\
J_{2,2} &= 4(+C_1 - 5C_2 + 8C_3 - 4C_4),\\
J_{2,3} &= 4(-C_1 + 7C_2 - 18C_3 + 20C_4 - 8C_5);\\
J_{4,0} &= 16(+C_2 - 2C_3 + C_4),\\
J_{4,1} &= 16(-C_2 + 4C_3 - 5C_4 + 2C_5),
\end{aligned} \tag{D16}$$

in which the integrals C_m can be expressed in terms of complete elliptic integrals of the first and second kind (F and E, respectively) with elliptic modulus k as

$$\begin{aligned}
C_0 &= \frac{\lambda}{3(1-k^2)}\left(-F + \frac{2(2-k^2)}{1-k^2}E\right),\\
C_1 &= \frac{\lambda}{3k^2(1-k^2)}\left(-F + \frac{1+k^2}{1-k^2}E\right),\\
C_2 &= \frac{\lambda}{3k^4(1-k^2)}\left((2-3k^2)F + \frac{2(2k^2-1)}{1-k^2}E\right),\\
C_3 &= \frac{\lambda}{3k^6(1-k^2)}\left((8-9k^2)F - \frac{3k^4-13k^2+8}{1-k^2}E\right),
\end{aligned}$$

$$C_4 = \frac{\lambda}{3k^8(1-k^2)}\left((16-16k^2-k^4)F - \frac{2k^6+4k^4-24k^2+16}{1-k^2}E\right),$$
$$C_5 = \frac{\lambda}{15k^{10}(1-k^2)}\left(128-120k^2-9k^4-4k^6)F - \frac{8k^8+11k^6+27k^4-184k^2+128}{1-k^2}E\right). \tag{D17}$$

APPENDIX E: TRANSLATING UNIT SPHERE

Following the example of Cortez *et al.* [12], consider the translating unit sphere with velocity $\mathbf{u} = -\hat{\mathbf{z}}$. The sphere is parametrized and discretized in the same manner as in Sec. III A. Assuming the sphere experiences zero-azimuthal spin, the fluid velocity at any point $\mathbf{x}_0$ can be approximated using the N ringlets via Eq. (22). Using intervals of equal size, the quadrature weight associated with numerical integration over $\mathbf{p}$ is simply $w_n = \frac{\pi}{N}\,\forall\, n$. Now considering the velocity evaluated at the location of each ring in the r-z plane yields a system of equations which can be written in matrix form

$$\mathsf{U} = \frac{1}{8N\mu}\begin{bmatrix}\mathsf{R}^{\varepsilon}_{rr} & \mathsf{R}^{\varepsilon}_{rz}\\ \mathsf{R}^{\varepsilon}_{zr} & \mathsf{R}^{\varepsilon}_{zz}\end{bmatrix}\mathsf{G}^{a}, \tag{E1}$$

as outlined in Eqs. (24)–(26). By setting

$$g^a_r(\mathbf{x}_i) = 0, \quad g^a_z(\mathbf{x}_i) = \frac{3\mu}{2a}U\,\forall\, i = 1,\ldots,N, \tag{E2}$$

where μ, a, and U are the fluid viscosity, sphere radius, and sphere speed (in z), respectively, the classical solution for Stokes flow

$$u_r(\mathbf{x}_i) = 0, \quad u_z(\mathbf{x}_i) = U\,\forall\, i = 1,\ldots,N, \tag{E3}$$

should follow. Note that this calculation is independent of the value of μ by cancellation (besides the implicit requirement that $\mathrm{Re} = UL/\mu \ll 1$ for the Stokes equations to be valid) and that we use $a = 1$ and $U = -1$ as described in the outline of the problem.

The first test involves using $N = 50$ regularized rings so that the grid size is given by $\pi/50 \approx 0.065$. This is chosen such that the minimum distance between adjacent rings in the axisymmetric discretization of the sphere surface is approximately the same as the distance between adjacent points in the discretization of Cortez *et al.* using $3N^2/2$ regularized Stokeslets. The regularization parameter ε is varied between 0.005 and 0.1, and the error in the ℓ^2 norm for the z component of the flow field is recorded in each case. This error is defined as

$$|u_z + 1|_2 := \sqrt{\frac{\sum_{i=1}^{N}[u_z(\mathbf{x}_i)+1]^2}{N}}. \tag{E4}$$

Division by N is necessary for the sake of comparison of errors with later tests where the value of N will change in order to alter the grid size. Initial results using regularized ringlets are shown in Fig. 15 and are favorable compared to those using regularized Stokeslets. The regularized ringlet method appears to be optimal for a lower value of ε than the regularized Stokeslet method, with a minimal error found at $\varepsilon \approx 0.015$ with our method and $\varepsilon \approx 0.025$ with that of the regularized Stokeslet, as well as being slightly more accurate for almost all values of ε tested. Interestingly, the magnitude of the errors using the two methods briefly appear to coincide near the point at which the regularized Stokeslet error is minimized.

The second test involves varying the grid size for a fixed value of $\varepsilon = 0.01$. Regularized ringlet results are shown in Fig. 16 and again compare very favorably to results using regularized Stokeslets. For larger grid sizes our errors are significantly reduced compared to those found using regularized Stokeslets. This is at least in part a result of the ringlet method being better suited to handling the

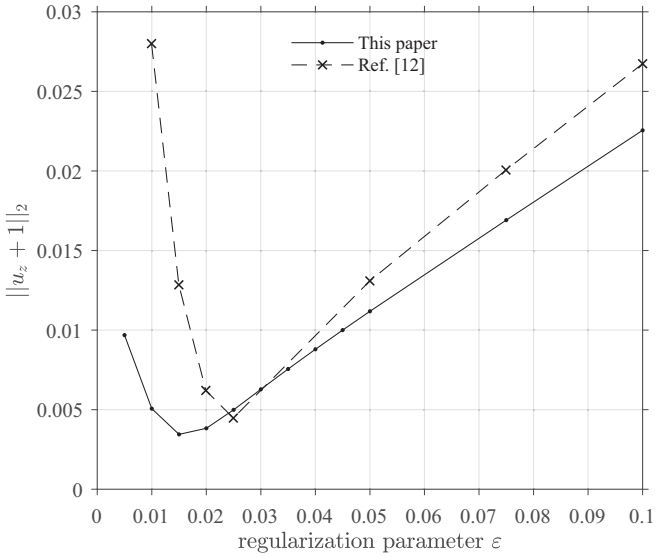

FIG. 15. Plot of ℓ^2 errors for various values of ε using $N = 50$ regularized Stokeslet rings in our discretization of the sphere surface (solid line), plotted against data taken from Ref. [12] (dashed line).

small value of $\varepsilon = 0.01$. With both methods, the error eventually stops decreasing as the grid size tends towards zero since in this regime the regularization error dominates.

The final test again looks at the effect of varying the value of ε on the magnitude of the numerical error, this time using $N = 124$ ringlets for a grid size approximately equal to 0.026 [note that we do not use $N = 125$ ringlets to avoid placing a ring at the point $(r, z) = (1, 0)$, which would result in a

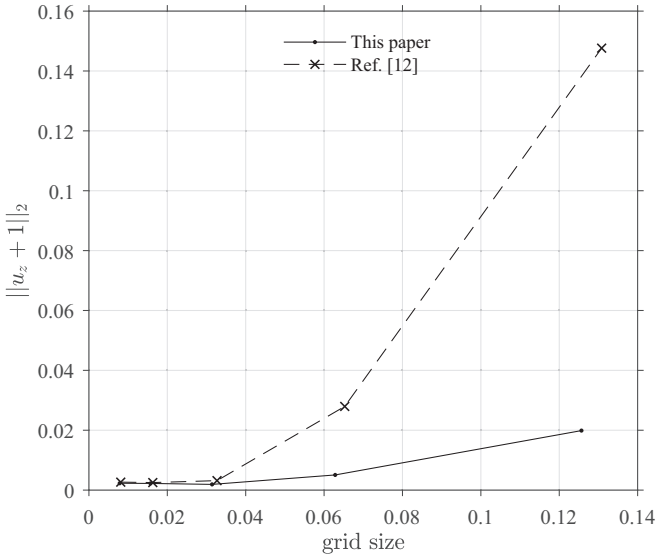

FIG. 16. Plot of ℓ^2 errors for different grid sizes ($N = 25, 50, 100, 200, 400$) in our regularized ring discretization of the sphere surface using fixed $\varepsilon = 0.01$ (solid line), plotted against data taken from Ref. [12] (dashed line).

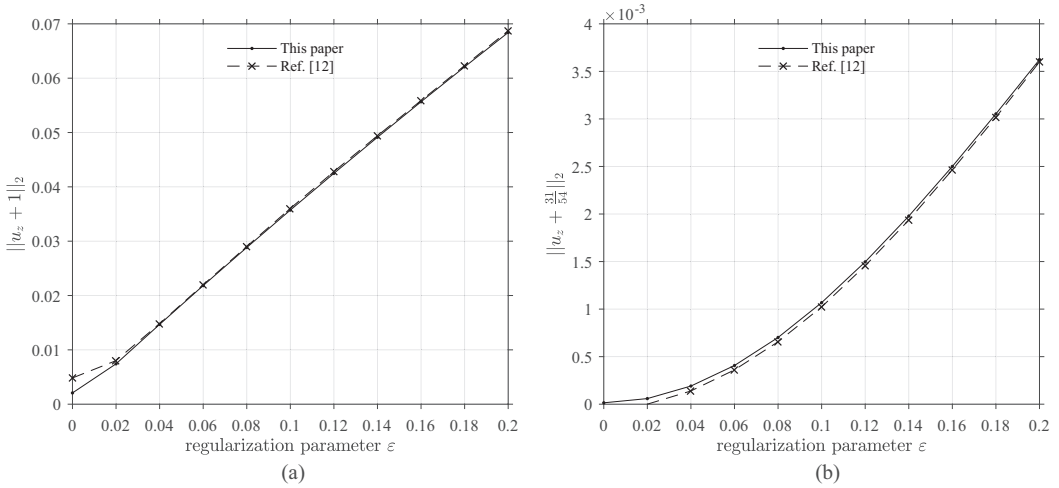

FIG. 17. Plot of ℓ^2 errors at surface point (a) $(r, z) = (1, 0)$ and (b) $(r, z) = (1.5, 0)$ for various values of ε using $N = 124$ regularized Stokeslet rings in our discretization of the sphere surface (solid line), plotted against data taken from Ref. [12] (dashed line).

singular velocity when $\varepsilon = 0$]. The velocity error is compared at two distinct points: $(r, z) = (1, 0)$ lying on the surface of the sphere and $(r, z) = (1.5, 0)$ lying a distance of half the sphere radius away. Ringlet results are shown in Figs. 17(a) and 17(b) and once more match regularized Stokeslet results very closely. The magnitude of the error is linear with respect to ε on the surface of the sphere and quadratic a sufficient distance away.

APPENDIX F: COMPARISON TO SINGULAR SOLUTIONS

Regularized solutions for Stokes flow have the advantage of being simple to implement and readily usable without needing to worry about the presence of singularities in the computational domain. This does not mean that singular solutions cannot be used however; so long as the appropriate care is taken to deal with the singularities in some way, singular solutions can also yield excellent results. The method of fundamental solutions [22,44] is a popular choice for implementing singular Stokeslet solutions, in which a fictitious boundary is placed outside of the computational domain and adjacent to the physical boundary of the problem considered. Stokeslets (or source points) are placed on this fictitious boundary and are associated with collocation points (typically of an equal number) on the physical boundary, with the force density for each Stokeslet being calculated using the resistance matrix such that the physical boundary conditions are satisfied. What the appropriate distance between the fictitious and physical boundaries should be is difficult to determine *a priori*, and in some sense this distance can be regarded as a regularization parameter for the singular problem [45]. If the separation distance is too small, the proximity between the Stokeslet singularities and the physical boundary may lead to inaccurate solutions, whereas if the distance is too large the resistance matrix may become ill-conditioned [46]. In some cases, placement of the fictitious boundary may also be constrained by the geometry of the problem itself, leading to solutions that are far from optimal. The difficulty in balancing all of these factors is one of the reasons for the popularity of regularized methods.

In the case of the axisymmetric ring of singular Stokeslets, some interesting behavior occurs in the limit as the source and collocation points coincide. In this limit, k tends to unity, from which it follows that $F \to \infty$ and $E \to 1$ in Eqs. (48)–(52). By employing the asymptotic expansion $F \approx -\ln \hat{r} + \cdots$ in which $\hat{r} = |\mathbf{x}_0 - \mathbf{x}_n|$, we find that $R^0_{\theta\theta} \approx 2R^0_{rr} \approx 2R^0_{zz} \approx -4 \ln \hat{r} + \cdots$ which all tend to infinity as $\hat{r} \to 0$ but at a significantly slower rate than the individual Stokeslet (approximately

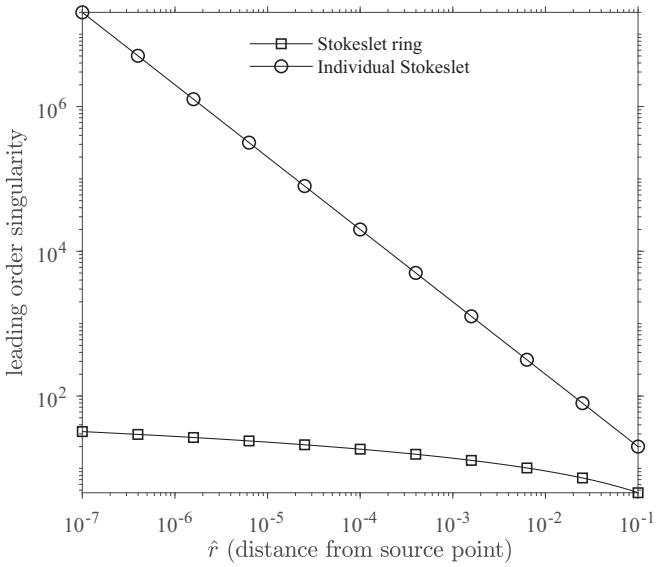

FIG. 18. Comparison of the magnitude of the singularities present in the Stokeslet (squares) and the Stokeslet ring (circles) in the limit as the source and collocation point coincide.

equal to $\hat{r}^{-1}$). The matrix elements R^0_{rz} and R^0_{zr} are similarly divergent but typically take values in the range $[-1, 1]$. Figure 18 shows a comparison of the magnitude of the singularities as $\hat{r} \to 0$ for $R^0_{rr}, R^0_{zz} \approx -2\ln\hat{r}$ (circles) versus $S^0_{ij} \approx 2\hat{r}^{-1}$ for $i = j$ (squares). A log-log plot must be employed due to the speed with which the Stokeslet singularity increases for small $\hat{r}$.

As a result of the slow rate with which the singularity in the axisymmetric Stokeslet ring approaches infinity, the method of fundamental solutions can be employed with a separation distance between the fictitious and physical boundaries that is several orders of magnitude smaller than is possible using individual Stokeslets. This allows for the discovery of accurate solutions with a well-conditioned underlying resistance matrix. We illustrate this by once again conducting MATLAB simulations for the resistance problem on the translating unit sphere (velocity $-\hat{\mathbf{z}}$) using both regularized and singular Stokeslet rings.

As before, the sphere is parametrized in two dimensions using the arc segment $\mathbf{p} = \cos\varphi\,\hat{\mathbf{r}} + \sin\varphi\,\hat{\mathbf{z}}$ for $\varphi \in [-\pi/2, \pi/2]$ with $N = 400$ points placed along its length at locations $\mathbf{x}_n$. For the method regularized ringlets, these $\mathbf{x}_n$ denote ringlet locations. The velocity $\mathbf{u}(\mathbf{x}_n) = -\hat{\mathbf{z}}$ is prescribed at all ringlet locations and the resistance matrix is constructed to yield the required force densities $\mathbf{g}^l(\mathbf{x}_n)$. The condition number of the resistance matrix R^ε is determined using the `cond` function in MATLAB. The analytical solution for the drag on the unit sphere with unit velocity $-\hat{\mathbf{z}}$ is known to be equal to $(3/2)\hat{\mathbf{z}}$, so the mean relative error for the calculation of the force term resulting from the resistance matrix is given by

$$e\left(g^a_z\right) = \frac{1}{N}\sum_{n=1}^{N}\left|\frac{g^a_z(\mathbf{x}_n) + 3/2}{-3/2}\right|, \tag{F1}$$

in which we recall that $\mathbf{g}^a$ is the force per unit area exerted by the sphere on the fluid and so has opposite sign to the drag. The fluid velocity at the near- and far-field locations $(r, z) = (0, 1.1), (0, 1.5)$ is evaluated using the force densities $\mathbf{g}^a$ according to Eq. (22). The relative error in these velocities is given by

$$e(1.1) = \left|\frac{u_z(0, 1.1) + 1315/1331}{-1315/1331}\right|, \quad e(1.5) = \left|\frac{u_z(0, 1.5) + 23/27}{-23/27}\right|, \tag{F2}$$

TABLE V. Accuracy of the method of regularized ringlets for various values of the regularization parameter ε in the resistance problem on the translating unit sphere. Columns refer to relative errors in total drag on the sphere $e(g_z^a)$, fluid velocity at the point $(r, z) = (0, 1.1)$ denoted by $e(1.1)$ and analogous error at (0,1.5), and finally the condition number of the underlying resistance matrix.

ε	$e(g_z^a)$	$e(1.1)$	$e(1.5)$	Condition No.
0.1	5.3	4.0×10^{-3}	1.7×10^{-2}	1.1×10^{19}
0.05	1.8×10^{-2}	2.5×10^{-3}	8.4×10^{-3}	8.6×10^{15}
0.025	9.7×10^{-3}	1.4×10^{-4}	4.1×10^{-3}	2.9×10^{10}
0.01	4.3×10^{-3}	5.8×10^{-4}	1.6×10^{-3}	4.2×10^{5}
0.005	2.5×10^{-3}	2.2×10^{-4}	7.6×10^{-4}	1.4×10^{4}
0.0025	2.1×10^{-3}	2.3×10^{-4}	1.1×10^{-4}	2.8×10^{3}
0.001	2.5×10^{-3}	1.0×10^{-3}	7.4×10^{-4}	1.0×10^{3}

based on the analytical solution given by Cortez *et al.* [12]. Table V shows a summary of the results obtained for each of these four metrics for various values of regularization parameter ε.

For the method of fundamental solutions, let $\mathbf{x}_n$ denote collocation points on the sphere surface; N source points are placed at positions $\mathbf{x}_s = (1 - 10^{-b}) \cdot \mathbf{x}_c$, where b is a parameter that represents the separation distance between the physical and fictitious boundaries (Fig. 19). The velocity $\mathbf{u}(\mathbf{x}_n) = -\hat{\mathbf{z}}$ is prescribed at all collocation points and the resistance matrix is constructed to yield the required force densities $\mathbf{g}^l(\mathbf{x}_s)$ at each source point. The accuracy and applicability of the method is measured using the same four metrics as for the method of regularized ringlets. Table VI shows a summary of results for various values of separation distance 10^{-b}, analogous to the results in the regularized case from Table V.

Similar results are achievable using both methods, although the singular method generally yields more well-conditioned resistance matrices and can produce relative errors of a smaller magnitude for the drag calculation and fluid velocities. It should however be noted that it is not possible to minimize each error in the singular calculation concurrently [as the smallest values for $e(1.1)$ and $e(1.5)$ are generally associated with larger values for the condition number and $e(g_z^a)$]. Despite axisymmetry enabling a drastic reduction of the separation distance for the singular problem, the question of what distance is considered optimal still persists. This is not an issue for the regularized ringlet, in which case each error achieves a minimal value for similar values of ε ($\approx$0.0025–0.005). For excessively small ε ($<$0.05), the error becomes nonmonotonic as is often the case with regularized Stokeslet methods (see, e.g., Fig. 15 and Refs. [12,26]). The same is also true for small b in the singular case. For both regularized and singular methods, reduction of the

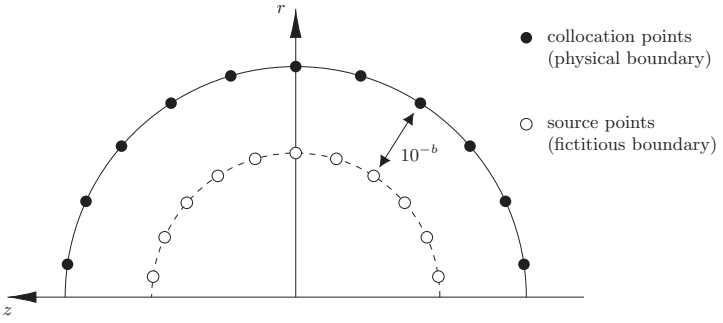

FIG. 19. Schematic diagram for implementation of the method of fundamental solutions on the unit sphere using singular rings in the r-z plane. Separation distance 10^{-b} is exaggerated for the sake of clarity.

TABLE VI. Accuracy of the method of fundamental solutions using singular ringlets for various values of the separation distance 10^{-b} in the resistance problem on the translating unit sphere. Columns refer to relative errors in total drag on the sphere $e(g_z^a)$, fluid velocity at the point $(r, z) = (0, 1.1)$ denoted by $e(1.1)$ and analogous error at (0,1.5), and finally the condition number of the underlying resistance matrix.

b	$e(g_z^a)$	$e(1.1)$	$e(1.5)$	Condition No.
1	4.8×10^{1}	1.5×10^{-13}	3.5×10^{-14}	1.1×10^{19}
2	1.6×10^{-2}	1.6×10^{-6}	3.8×10^{-7}	9.5×10^{6}
3	4.3×10^{-3}	9.5×10^{-4}	6.3×10^{-4}	2.5×10^{3}
4	5.4×10^{-4}	3.0×10^{-3}	2.5×10^{-3}	4.4×10^{2}
5	7.3×10^{-3}	5.1×10^{-3}	4.6×10^{-3}	2.4×10^{2}
6	9.4×10^{-3}	7.2×10^{-3}	6.7×10^{-3}	1.6×10^{2}
7	1.1×10^{-2}	9.3×10^{-3}	8.8×10^{-3}	1.2×10^{2}

regularization parameter ε or b always appears to result in a reduction of the condition number of the resistance matrix.

Although the singular method can be tuned to give smaller relative errors in either the fluid velocity or total drag separately, it cannot do so simultaneously; regularized ringlets display more satisfactory convergence properties and are the more effective method to minimize errors in both fluid velocity and total drag.

APPENDIX G: MEASURING COMPUTATIONAL SPEED

Table VII shows a comparison of the computational times t_R and t_S (measured in seconds), associated with constructing the $2N \times 2N$ ringlet matrix R^ε (in the zero-azimuthal-velocity fluid case) and the $3N \times 3N$ Stokeslet matrix S^ε, respectively. The increase in computational time for computing R^ε is a result of needing to compute the complete elliptic integrals $F(k)$ and $E(k)$ for all combinations of ring locations $(\mathbf{x}_m, \mathbf{x}_n)\,\forall\, m, n \in 1, \ldots, N$, which requires the construction of two further $2N \times 2N$ matrices E and F. The computational time needed for this isolated operation t_e is also listed in Table VII. The total additional time needed to construct R^ε is modest, typically between 10% and 20% of the time needed for S^ε.

The computational time associated with F and E (and by extension R^ε) can be reduced by evaluating $F(k)$ and $E(k)$ to a lower degree of accuracy; the MATLAB function `ellipke(k,TOL)` calculates $F(k)$ and $E(k)$ to the accuracy defined by `TOL`, which has a default value of $2^{-52} \approx 2.2 \times 10^{-16}$ (double-precision accuracy). This is a far greater accuracy than we are typically able to achieve using regularized Stokeslet methods, suggesting a larger value of `TOL` will suffice.

We note that by consideration of the size of the matrices involved and the typically small value of t_e, we should hypothetically be able to achieve $t_R = (4/9)t_S + t_e < t_S$ for any given value of N. In practice, this is not the case. The elements S_{ij}^ε for $i, j \in \{1, 2, 3\}$ share a common form that enables them to be encoded in matrix form S^ε very efficiently. The same is not true of the elements $R_{\alpha\beta}^\varepsilon$ for $\alpha, \beta \in \{r, z\}$ and hence why $t_R > t_S\,\forall N$ in Table VII.

TABLE VII. Comparison of computational time for evaluating elliptic integrals as well as constructing ring matrix R^ε and Stokeslet matrix S^ε using varying numbers of nodes.

Time (s)	$N = 1000$	$N = 2000$	$N = 3000$	$N = 4000$	$N = 5000$	$N = 6000$
t_e	0.1029	0.4100	0.9208	1.6228	2.5303	3.6553
t_R	0.2863	1.1182	2.4406	4.4124	6.9682	9.9643
t_S	0.2380	0.9396	2.1676	3.7562	6.0355	8.9524

TABLE VIII. Computational time associated with solving the linear system $\mathbf{X} = \mathbf{A}\backslash\mathbf{b}$ for varying sizes of matrix $\mathbf{A}$ and vector $\mathbf{b}$.

Time (s)	$N = 1000$	$N = 2000$	$N = 3000$	$N = 4000$	$N = 5000$	$N = 6000$
t_N	0.0178	0.1119	0.2986	0.6377	1.2263	2.0053
t_{2N}	0.1018	0.7139	2.0614	5.1004	9.3121	15.7495
t_{3N}	0.2978	2.3084	6.7434	15.1372	30.0496	50.7495

Inclusion of azimuthal flow (such that an additional $N \times N$ matrix must be constructed for $\mathsf{R}_\theta^\varepsilon$) incurs an additional cost of small value, approximately equal to $(t_R - t_e)/4$ for any given value of N. We divide by 4 under the assumption that the cost associated with constructing the additional $N \times N$ matrix $\mathsf{R}_\theta^\varepsilon$ is one-quarter of the cost associated with constructing the zero-azimuthal $2N \times 2N$ matrix R^ε.

The true value of working with ringlets can be seen by evaluating the cost of inverting the matrices $\mathsf{R}_\theta^\varepsilon$ and R^ε versus S^ε (as is necessary in the resistance problem for evaluating the force associated with a given boundary velocity). These matrices are of size $N \times N$, $2N \times 2N$, and $3N \times 3N$, respectively. We investigate the cost of solving a linear system $\mathbf{X} = \mathbf{A}\backslash\mathbf{b}$ in which $\mathbf{A}$ and $\mathbf{b}$ are an $M \times M$ matrix and an $M \times 1$ vector of normally distributed random data, respectively, with $M \in \{N, 2N, 3N\}$. We denote the time taken to solve this system by t_N, t_{2N}, and t_{3N} in each case. The results are given in Table VIII, in which it is clear to see that t_{3N} is significantly larger than the sum of t_N and t_{2N} for all values of N tested. In practice, this means that using a 3D Stokeslet implementation with S^ε for solving an axisymmetric resistance problem will always be significantly more costly than our 2D ringlet implementation with R^ε and $\mathsf{R}_\theta^\varepsilon$.

As well as producing smaller resistance matrices with a reduced associated computational cost for a given number of nodes, our axisymmetric ringlet method also requires far fewer nodes in order to achieve the same level of accuracy as the traditional regularized Stokeslet method. In Appendix E it was shown that for the case of the translating unit sphere the axisymmetric discretization of the sphere surface with N rings produces results that are consistently more accurate than the traditional 3D patch discretization using $3N^2/2$ nodes. The result using 1000 ringlets in two dimensions (computational time approximately equal to 0.1 s) thus corresponds to using 1 500 000 regularized Stokeslets in three dimensions (computational time approximately equal to 500 days, extrapolating from data in Table VIII and assuming that $t_{3N} \propto N^{2.6}$ such that doubling N corresponds to a sixfold increase in t_{3N}), a drastic improvement in computational efficiency.

APPENDIX H: FORCE CALCULATION FOR THE ROTATING SPHERE

The expression for the torque on the rotating sphere in a Stokesian fluid is given by

$$\mathbf{T} = -8\pi\mu a^3\boldsymbol{\Omega}, \tag{H1}$$

the derivation of which can be found in [28]. This torque is associated with a drag force per unit area on the surface of the sphere given by $\mathbf{f} = -3\mu\omega_0(r/a)\hat{\boldsymbol{\theta}}$, which can be verified by considering the identity

$$\mathbf{T} = \iint_S \mathbf{x} \times \mathbf{f}\, dS, \tag{H2}$$

where S denotes the sphere surface. Multiplication by $\hat{\mathbf{z}}$ yields

$$-8\pi\mu a^3\omega_0 = \hat{\mathbf{z}} \cdot \iint_S \mathbf{x} \times \mathbf{f}\, dS. \tag{H3}$$

In cylindrical coordinates, we have

$$\hat{\mathbf{z}} \cdot (\mathbf{x} \times \mathbf{f}) = \hat{\mathbf{z}} \cdot \{(r\hat{\mathbf{r}} + \theta\hat{\boldsymbol{\theta}} + z\hat{\mathbf{z}}) \times [-3\mu\omega_0(r/a)\hat{\boldsymbol{\theta}}]\} = -3\mu\omega_0(r/a)\hat{\mathbf{z}} \cdot (r\hat{\mathbf{z}} - z\hat{\mathbf{r}}) = -3\mu\omega_0(r^2/a). \tag{H4}$$

Converting to a spherical system (r, θ, φ) in which θ denotes the azimuthal angle and φ the polar angle, we substitute $r^2 = a^2 \sin^2\varphi$ and $dS = a^2 \sin\varphi \, d\theta d\varphi$ such that

$$\begin{aligned}\hat{\mathbf{z}} \cdot \iint_S \mathbf{x} \times \mathbf{f} \, dS &= -3\mu a^3 \omega_0 \int_{\theta=0}^{2\pi} \left(\int_{\varphi=0}^{\pi} \sin^3\varphi \, d\varphi \right) d\theta = -6\pi\mu a^3 \omega_0 \int_{\varphi=0}^{\pi} \sin^3\varphi \, d\varphi \\ &= -6\pi\mu a^3 \omega_0 \frac{4}{3} = -8\pi\mu a^3 \omega_0, \end{aligned} \tag{H5}$$

as required.

[1] E. Lauga and T. R. Powers, The hydrodynamics of swimming microorganisms, Rep. Prog. Phys. **72**, 096601 (2009).

[2] N. Phan-Thien, T. Tran-Cong, and M. Ramia, A boundary-element analysis of flagellar propulsion, J. Fluid Mech. **184**, 533 (1987).

[3] M. Ramia, D. Tullock, and N. Phan-Thien, The role of hydrodynamic interaction in the locomotion of microorganisms, Biophys. J. **65**, 755 (1993).

[4] H. Shum, E. A. Gaffney, and D. J. Smith, Modelling bacterial behavior close to a no-slip plane boundary: The influence of bacterial geometry, Proc. R. Soc. A **466**, 1725 (2010).

[5] A. T. Chwang and T. Y.-T. Wu, Hydromechanics of low-Reynolds-number flow. Part 2. Singularity method for Stokes flows, J. Fluid Mech. **67**, 787 (1975).

[6] A. T. Chwang and T. Y.-T. Wu, Hydromechanics of low-Reynolds-number flow. Part 1. Rotation of axisymmetric prolate bodies, J. Fluid Mech. **63**, 607 (1974).

[7] A. T. Chwang, Hydromechanics of low-Reynolds-number flow. Part 3. Motion of a spheroidal particle in quadratic flows, J. Fluid Mech. **72**, 17 (1975).

[8] A. T. Chwang and T. Y. Wu, Hydromechanics of low-Reynolds-number flow. Part 4. Translation of spheroids, J. Fluid Mech. **75**, 677 (1976).

[9] R. E. Johnson and T. Y. Wu, Hydromechanics of low-Reynolds-number flow. Part 5. Motion of a slender torus, J. Fluid Mech. **95**, 263 (1979).

[10] L. H. Huang and A. T. Chwang, Hydromechanics of low-Reynolds-number flow. Part 6. Rotation of oblate bodies, J. Eng. Math. **20**, 307 (1986).

[11] R. Cortez, The method of regularized Stokeslets, SIAM J. Sci. Comput. **23**, 1204 (2001).

[12] R. Cortez, L. Fauci, and A. Medovikov, The method of regularized Stokeslets in three dimensions: analysis, validation, and application to helical swimming, Phys. Fluids **17**, 031504 (2005).

[13] D. J. Smith, A boundary element regularized Stokeslet method applied to cilia- and flagella-driven flow, Proc. R. Soc. A **465**, 3605 (2009).

[14] R. Cortez, Regularized Stokeslet segments, J. Comput. Phys. **375**, 783 (2018).

[15] D. J. Smith, A nearest-neighbour discretisation of the regularized stokeslet boundary integral equation, J. Comput. Phys. **358**, 88 (2018).

[16] J. R. Blake, A spherical envelope approach to ciliary propulsion, J. Fluid Mech. **46**, 199 (1971).

[17] E. M. Purcell, Life at low Reynolds number, Am. J. Phys. **45**, 3 (1977).

[18] Y. Chebli, J. Kroeger, and A. Geitmann, Transport logistics in pollen tubes, Mol. Plant **6**, 1037 (2013).

[19] C. Pozrikidis, *Boundary Integral and Singularity Methods for Linearized Viscous Flow* (Cambridge University Press, Cambridge, 1992).

[20] A. M. Leshansky and O. Kenneth, Surface tank treading: Propulsion of Purcell's toroidal swimmer, Phys. Fluids **20**, 063104 (2008).

[21] G. Fairweather and A. Karageorghis, The method of fundamental solutions for elliptic boundary value problems, Adv. Comput. Math. **9**, 69 (1998).

[22] D. L. Young, S. J. Jane, C. M. Fan, K. Murugesan, and C. C. Tsai, The method of fundamental solutions for 2D and 3D Stokes problems, J. Comput. Phys. **211**, 1 (2006).
[23] I. S. Gradshteyn and I. M. Ryzhik, *Table of Integrals, Series, and Products* (Academic, USA, 2014).
[24] K. Leiderman, E. L. Bouzarth, R. Cortez, and A. T. Layton, A regularization method for the numerical solution of periodic Stokes flow, J. Comput. Phys. **236**, 187 (2013).
[25] H.-N. Nguyen and R. Cortez, Reduction of the regularization error of the method of regularized Stokeslets for a rigid object immersed in a three-dimensional Stokes flow, Commun. Comput. Phys. **15**, 126 (2014).
[26] M. T. Gallagher, D. Choudhuri, and D. J. Smith, Sharp quadrature error bounds for the nearest-neighbor discretization of the regularized stokeslet boundary integral equation, SIAM J. Sci. Comput. **41**, B139 (2019).
[27] H. Lamb, *Hydrodynamics* (Courier Corporation, Chelmsford, 1945), Chap. XI.
[28] S. I. Rubinow and J. B. Keller, The transverse force on a spinning sphere moving in a viscous fluid, J. Fluid Mech. **11**, 447 (1961).
[29] R. M. Thaokar, H. Schiessel, and I. M. Kulic, Hydrodynamics of a rotating torus, Eur. Phys. J. B **60**, 325 (2007).
[30] G. I. Taylor, Analysis of the swimming of long and narrow animals, Proc. R. Soc. London Ser. A **214**, 158 (1952).
[31] I. Kulić, R. Thaokar, and H. Schiessel, Twirling DNA rings-Swimming nanomotors ready for a kickstart, Europhys. Lett. **72**, 527 (2005).
[32] Jiro (MathWorks staff), GRABIT function (File Exchange), https://uk.mathworks.com/matlabcentral/fileexchange/7173-grabit, accessed 12 October 2018.
[33] J. Bove, B. Vaillancourt, J. Kroeger, P. K. Hepler, P. W. Wiseman, and A. Geitmann, Magnitude and direction of vesicle dynamics in growing pollen tubes using spatiotemporal image correlation spectroscopy and fluorescence recovery after photobleaching, Plant Physiol. **147**, 1646 (2008).
[34] G. Booy, F. A. Krens, and R. J. Bino, Analysis of pollen-tube growth in cultured maize silks, Sexual Plant Reprod. **5**, 227 (1992).
[35] P. Fayant, O. Girlanda, Y. Chebli, C.-É. Aubin, I. Villemure, and A. Geitmann, Finite element model of polar growth in pollen tubes, Plant Cell **22**, 2579 (2010).
[36] J. Dumais, S. L. Shaw, C. R. Steele, S. R. Long, and P. M. Ray, An anisotropic-viscoplastic model of plant cell morphogenesis by tip growth, Int. J. Dev. Biol. **50**, 209 (2006).
[37] A. Lovy-Wheeler, K. L. Wilsen, T. I. Baskin, and P. K. Hepler, Enhanced fixation reveals the apical cortical fringe of actin filaments as a consistent feature of the pollen tube, Planta **221**, 95 (2005).
[38] Y. Fu, G. Wu, and Z. Yang, ROP GTPase-dependent dynamics of tip-localized F-actin controls tip growth in pollen tubes, J. Cell Biol. **152**, 1019 (2001).
[39] L. Vidali, S. T. McKenna, and P. K. Hepler, Actin polymerization is essential for pollen tube growth, Mol. Biol. Cell **12**, 2534 (2001).
[40] X. Wang, Y. Teng, Q. Wang, X. Li, X. Sheng, M. Zheng, J. Šamaj, F. Baluška, and J. Lin, Imaging of dynamic secretory vesicles in living pollen tubes of *Picea meyeri* using evanescent wave microscopy, Plant Physiol. **141**, 1591 (2006).
[41] I. Y. Wong, M. L. Gardel, D. R. Reichman, E. R. Weeks, M. T. Valentine, A. R. Bausch, and D. A. Weitz, Anomalous Diffusion Probes Microstructure Dynamics of Entangled F-Actin Networks, Phys. Rev. Lett. **92**, 178101 (2004).
[42] A. H. N. De Win, Quantitative analysis of organelle movements in pollen tubes, Ph.D. thesis, Radboud University, 1997.
[43] J. Huang and L. Fauci, Interaction of toroidal swimmers in Stokes flow, Phys. Rev. E **95**, 043102 (2017).
[44] C. J. S. Alves and A. L. Silvestre, Density results using Stokeslets and a method of fundamental solutions for the Stokes equations, Eng. Anal. Bound. Elem. **28**, 1245 (2004).
[45] A. Barrero-Gil, The method of fundamental solutions without fictitious boundary for solving Stokes problems, Comput. Fluids **62**, 86 (2012).
[46] C. W. Chen, D. L. Young, C. C. Tsai, and K. Murugesan, The method of fundamental solutions for inverse 2D Stokes problems, Comput. Mech. **37**, 2 (2005).